Supporting Information

Sublimable Single Ion Magnets Based on Lanthanoid Quinolinate Complexes: The Role of Intermolecular Interactions on Their Thermal Stability

Walter Cañon-Mancisidor,[1,2,3*] Sara G. Miralles,[1] José J. Baldoví,[4] Guillermo Mínguez Espallargas,[1] Alejandro Gaita-Ariño,[1] Eugenio Coronado[1*]

[1] Instituto de Ciencia Molecular (ICMol), Universitat de València, c/ Catedrático José Beltrán, 2, E-46980 Paterna, Spain.

[2] Facultad de Química y Biología, Depto. de Química dex los Materiales, Universidad de Santiago de Chile, USACH, Av. Lib Bernardo O´Higgins 3363, Estación Central, CP-9170022, Chile.

[3] Center for the Development of Nanoscience and Nanotechnology, CEDENNA, Av. Lib Bernardo O´Higgins 3363, Estación Central, CP-9170022, Chile.

[4] Max Planck Institute for the Structure and Dynamics of Matter, Luruper Chaussee 149, D-22761 Hamburg, Germany.

E-mail: walter.canon@usach.cl; eugenio.coronado@uv.es

S.1. SYNTHESIS

A modified approach of the synthesis of lanthanide tetrakis complexes described by Van Deun and others was used[1–3] to obtain a family of pure tetrakis complexes of general formula, $Na[Ln(5,7-X_2q)_4]$. The ligands (Sigma-Aldrich) 5,7-dibromo-8-hydroxyquinoline (5,7-Br_2q) and 5,7-chloroiodo-8-hydroxyquinoline (5,7-ClIq) were recrystallized in $CHCl_3$. The rest of the chemicals were used without further purification.

Fourier transform infrared spectroscopy (FTIR) was performed using a NICOLET 5700 in the range of 4000 – 650 cm^{-1} for the powder and crystalline materials. ESI-mass spectra were obtained with a Waters Micromass ZQ spectrometer in the negative ion mode. In all cases, well-resolved isotopic patterns consisting of mono-isotopic peaks separated by 1/z Da were obtained. Elemental analyses (C, N, H) of bulk samples were performed by microanalytical procedures using an EA 1110 CHNS-O elemental analyzer from CE instruments. The Ln : X ratios (where X = Br, I, Cl) of the bulk material were estimated by electron probe microanalysis (EPMA) performed with a Philips SEM XL30 equipped with an EDAX DX-4 microprobe. Thermal analyses were done in Mettler Toledo TGA/SDTA 851e in the range 25 – 1000°C at rate of 10°C/min for all compounds.

S.1.1. Synthesis of $Na[Ln(5,7-Br_2q)_4]$ (1)

In 100 mL of absolute ethanol 4 mmol of the 5,7-Br_2q were dissolved under stirring. A solution of 4 mmol of NaOH dissolved in 20 mL of ethanol at 80°C was added. Then, a solution of 0.6 mmol of $LnCl_3 \cdot 6H_2O$ (Ln = Dy^{III}; Tb^{III}; Er^{III}; Ho^{III}) in hot absolute ethanol (20 mL) was slowly added dropwise. A yellow suspension was formed, and the suspension was kept under stirring at 80°C during 1 hour. Then, the solution was kept under stirring until the solution cooled down to room temperature. The suspension was filtered on a sintered-glass filter n°5 and a yellow precipitate was obtained, which were washed with 10 mL H_2O water and 10 mL of a cold mixture EtOH/H_2O [50:50] and then dried in the oven at 110°C for 24h. These solids were characterized as $Na[Ln(5,7-Br_2q)_4]$ (1) compounds.

Na[Dy(5,7-Br₂q)₄] **1(Dy)**, FTIR ν (cm−1): 1547 (s), 1482 (s), 1446 (s), 1388 (s), 1370 (s), 1353 (m), 1247 (w), 1213 (w), 1136(w), 1107 (m), 1047 (w), 936 (m), 870 (w), 857 (m), 806 (m), 786 (m), 742 (s), 682 (w), 665 (m). ES-MS in negative mode (DMF) m/z = 1370, which corresponds to the $[Dy(5,7-Br_2q)_4]^-$ anion. Elem. Anal. for $C_{36}H_{16}Br_8N_4O_4DyNa$; C = 31.0%, N = 4.0%, H = 1.1%; found C = 30.2%, N = 3.9%, H = 1.0%. Elemental ratio estimated by electron probe microanalysis (EPMA): (Exp) Teo Dy : Na : Br = (1.07)1 : (0.95)1 : (7.96)8. TG measurement shows mass losses at 220°C, 440°C and then the mass loss continues decreasing until a plateau is reach at 820°C.

Na[Tb(5,7-Br₂q)₄] **1(Tb)**, FTIR ν (cm−1): 1547 (s), 1482 (s), 1444 (s), 1388 (s), 1370 (s), 1353 (m), 1246 (w), 1213 (w), 1137 (w), 1105 (m), 1047 (w), 936 (m), 872 (w), 855 (m), 807 (m), 786 (m), 742 (s), 682 (w), 665 (m). ES-MS in negative mode (DMF) m/z = 1367, which corresponds to the $[Tb(5,7-Br_2q)_4]^-$ anion. Elem. Anal. for $C_{36}H_{16}Br_8N_4O_4TbNa$; C = 31.9%, N = 4.0%, H = 1.1%; found C = 31.5%, N = 3.9%, H = 1.0%. Elemental ratio estimated by electron probe microanalysis (EPMA): (Exp) Teo Tb : Na : Br = (0.96)1 : (1.05)1 : (7.97)8. TG measurement shows mass losses at 220°C, 440°C, 650°C and then the mass continues decreasing until a plateau is reach at 820°C.

Na[Er(5,7-Br₂q)₄] **1(Er)**, FTIR ν (cm−1): 1548 (s), 1482 (s), 1446 (s), 1388 (s), 1372 (s), 1353 (m), 1247 (w), 1213 (w), 1139 (w), 1107 (m), 1048 (w), 937 (m), 870 (w), 857 (m), 807 (m), 787 (m), 742 (s), 682 (w), 665 (m). ES-MS in negative mode (DMF) m/z = 1375, which corresponds to the $[Er(5,7-Br_2q)_4]^-$ anion. Elem. Anal. for $C_{36}H_{16}Br_8N_4O_4ErNa$; C = 30.9%, N = 4.0%, H = 1.1%; found C = 29.9%, N = 3.9%, H = 1.0%. Elemental ratio estimated by electron probe microanalysis (EPMA): (Exp) Teo Er : Na : Br = 0.98(1) : (0.95)1 : (7.87)8. TG measurement shows a similar thermal behavior than for **1(Dy)**.

Na[Ho(5,7-Br₂q)₄] **1(Ho)**, FTIR ν (cm−1): 1549 (s), 1482 (s), 1446 (s), 1388 (s), 1372 (s), 1355 (m), 1249 (w), 1215 (w), 1136 (w), 1107 (m), 1046 (w), 936 (m), 876 (w), 857 (m), 807 (m), 787 (m), 742 (s), 682 (w), 665 (m). ES-MS in negative mode (DMF) m/z = 1372, which corresponds to the $[Ho(5,7-Br_2q)_4]^-$ anion. Elem. Anal. for $C_{36}H_{16}Br_8N_4O_4HoNa$; C = 30.9%, N = 4.0%, H = 1.1%; found C = 30.5%, N = 3.9%, H = 0.8%. Elemental ratio estimated by electron probe microanalysis (EPMA): (Exp) Teo Ho : Na : Br = 1.02(1) : (0.95)1 : (8.04)8. TG measurement shows a similar thermal behavior than for **1(Dy)**.

S.1.2. Synthesis of $Na[Ln(5,7-ClIq)_4]$ (2)

In 100 mL of absolute ethanol 4 mmol of the 5,7-ClIq were dissolved under stirring. A solution of 4 mmol of NEt_3 were added to the ligand solution. In addition, 0.6 mmol of NaCl were dissolved in 2ml of H_2O and then about 18 mL extra of ethanol at 80°C was added. Then, a solution of 0.6 mmol of $LnCl_3 \cdot 6H_2O$ (Ln = Dy^{III}; Tb^{III}; Er^{III}; Ho^{III}; Y^{III}) in hot absolute ethanol (20 mL) was slowly added dropwise. A yellow suspension was formed, and the suspension was kept under stirring at 80°C during 1 hour. Then, the

solution was kept under stirring until the solution cooled down to room temperature. The suspension was filtered on a sintered-glass filter n°5 and a yellow precipitate was obtained, which were washed with 10 mL H_2O water and 10 mL of a cold mixture $EtOH/H_2O$ [50:50] and then dried in the oven at 110°C for 24h. These solids were characterized as $Na[Ln(5,7-ClIq)_4]$ (**2**) compounds.

Na[Dy(5,7-ClIq)₄] **2(Dy)**, FTIR ν (cm^{-1}): 1543 (s), 1482 (s), 1439 (s), 1388 (s), 1374 (s), 1355 (m), 1247 (w), 1213 (w), 1133 (w), 1105 (m), 1044 (w), 956 (m), 872 (w), 846 (w), 809 (m), 786 (m), 744 (s), 699 (w), 664 (m). ES-MS in negative mode (DMF) m/z = 1379, which corresponds to the $[Dy(5,7-ClIq)_4]^-$ anion. Elem. Anal. for $C_{36}H_{16}Cl_4I_4N_4O_4DyNa$; C = 30.8%; N = 3.9%; H = 1.2%; found C = 30.1%, N = 4.0%, H = 0.9%. Elemental ratio estimated by electron probe microanalysis (EPMA): (Exp) Teo Dy : Na : Cl : I = (0.93)1 : (1.14)1 : (3.94)4 : (4.01)4. TG measurement shows at 350 °C a vertical mass loss and after the mass loss mention before the thermal behavior is almost the same as for **1(Dy)**, showing mass losses at 520°C and 900°C.

Na[Tb(5,7-ClIq)₄] **2(Tb)**, FTIR ν (cm^{-1}): 1543 (s), 1482 (s), 1439 (s), 1388 (s), 1372 (s), 1355 (m), 1247 (w), 1213 (w), 1133 (w), 1105 (m), 1044 (w), 956 (m), 872 (w), 846 (w), 809 (m), 787 (m), 744 (s), 699 (w), 664 (m). ES-MS in negative mode (DMF) m/z = 1377, which corresponds to the $[Tb(5,7-ClIq)_4]^-$ anion. Elem. Anal. for $C_{36}H_{16}Cl_4I_4N_4O_4TbNa$; C = 30.9%; N = 4.0%; H = 1.2%; found C = 30.8%, N = 3.9%, H = 0.8%. Elemental ratio estimated by electron probe microanalysis (EPMA): (Exp) Teo Tb : Na : Cl : I = (0.95)1 : (1.06)1 : (3.91)4 : (4.09)4. TG measurement shows a similar thermal behavior to **2(Dy)**.

Na[Er(5,7-ClIq)₄] **2(Er)**, FTIR ν (cm^{-1}): 1545 (s), 1482 (s), 1439 (s), 1389 (s), 1372 (s), 1357 (m), 1245 (w), 1215 (w), 1135 (w), 1105 (m), 1046 (w), 956 (m), 870 (w), 846 (w), 807 (m), 785 (m), 744 (s), 699 (w), 664 (m). ES-MS in negative mode (DMF) m/z = 1386, which corresponds to the $[Er(5,7-ClIq)_4]^-$ anion. Elem. Anal. for $C_{36}H_{16}Cl_4I_4N_4O_4ErNa$; C = 30.7%; N = 3.9%; H = 1.2%; found C = 30.7%, N = 3.9%, H = 1.1%. Elemental ratio estimated by electron probe microanalysis (EPMA): (Exp) Teo Er : Na : Cl : I = (1.02)1 : (1.09)1 : (3.97)4 : (4.13)4. TG measurement shows a similar thermal behavior than for **2(Dy)**.

Na[Ho(5,7-ClIq)₄] **2(Ho)**, FTIR ν (cm−1): 1543 (s), 1482 (s), 1439 (s), 1388 (s), 1372 (s), 1357 (m), 1247 (w), 1213 (w), 1135 (w), 1105 (m), 1046 (w), 956 (m), 872 (w), 846 (w), 807 (m), 785 (m), 744 (s), 699 (w), 663 (m). ES-MS in negative mode (DMF) m/z = 1383, which corresponds to the $[Ho(5,7-ClIq)_4]^-$ anion. Elem. Anal. for $C_{36}H_{16}Cl_4I_4N_4O_4HoNa$; C = 30.8%; N = 3.9%; H = 1.2%; found C = 30.4%, N = 3.8%, H = 0.9%. Elemental ratio estimated by electron probe microanalysis (EPMA): (Exp) Teo Ho : Na : Cl : I = (0.89)1 : (1.13)1 : (3.92)4 : (3.98)4. TG measurement shows a similar thermal behavior than for **2(Dy)**.

S.1.3. Synthesis of Na[Ln(5,7-X₂q)₄]·DMF (1-DMF and 2-DMF)
150 mg of the dried yellow powder of the complexes **1** and **2** were dissolved in approximately 2 ml of hot DMF (100°C). Single crystals of *Na[Ln(5,7-Br₂q)₄]·DMF* **1-DMF** and *Na[Ln(5,7-ClIq)₄]·DMF* **2-DMF** appear after a few days. The chemical purities of all materials were confirmed by several characterization techniques.

Na[Dy(5,7-Br₂q)₄]·DMF **1-DMF(Dy)**, FTIR ν (cm−1): 1681 (s), 1550 (s), 1483 (s), 1450 (s), 1390 (s), 1373 (s), 1357 (m), 1249 (w), 1214 (w), 1137 (w), 1107 (m), 1049 (w), 939 (m), 875 (w), 858 (m), 809 (m), 786 (m), 742 (s), 684 (w), 667 (m). Elem. Anal. for $C_{39}H_{23}Br_8N_5O_5DyNa$; C = 31.9%, N = 4.8%, H = 1.6%; found C = 31.5%, N = 4.8%, H = 1.6%. Elemental ratio estimated by electron probe microanalysis (EPMA): (Exp) Teo Dy : Na : Br = (0.99)1 : (0.98)1 : (8.01)8. TG measurement shows weight losses at 220°C, a second mass loss is observed at approximately 460°C, and then as for 1a the mass loss continues decreasing until a plateau is reach at 800°C.

Na[Tb(5,7-Br₂q)₄]·DMF **1-DMF(Tb)**, FTIR ν (cm−1): 1679 (s), 1550 (s), 1483 (s), 1448 (s), 1390 (s), 1371 (s), 1355 (m), 1248 (w), 1215 (w), 1138 (w), 1107 (m), 1049 (w), 937 (m), 875 (w), 858 (m), 809 (m), 786 (m), 742 (s), 684 (w), 667 (m). Elem. Anal. for $C_{39}H_{23}Br_8N_5O_5TbNa$; C = 32.0%, N = 4.8%, H = 1.6%; found C = 31.9%, N = 4.8%, H = 1.4%. Elemental ratio estimated by electron probe microanalysis (EPMA): (Exp) Teo Tb : Na : Br = (0.98)1 : (1.01)1 : (8.00)8. TG measurement shows weight losses at 220°C, a second mass loss is observed at approximately 460°C. At 650°C the mass loss is less than for **1-DMF(Dy)**, but nevertheless as for **1-DMF(Tb)** the mass loss continues decreasing until a plateau is reach at 800°C.

Na[Er(5,7-Br₂q)₄]·DMF **1-DMF(Er)**, FTIR ν (cm−1): 1682 (s), 1552 (s), 1485 (s), 1450 (s), 1390 (s), 1373 (s), 1357 (m), 1250 (w), 1215 (w), 1138 (w), 1107 (m), 1051 (w), 939 (m), 875 (w), 858 (m), 809 (m), 787 (m), 744 (s), 684 (w), 667 (m). Elem. Anal. for $C_{39}H_{23}Br_8N_5O_5ErNa$; C = 31.8%, N = 4.8%, H = 1.6%; found C = 31.4%, N = 4.8%, H = 1.5%. Elemental ratio estimated by electron probe microanalysis (EPMA): (Exp) Teo Er : Na : Br = (1.01)1 : (0.99)1 : (7.98)8. TG measurement shows a similar thermal behavior than for **1-DMF(Dy)**.

Na[Ho(5,7-Br$_2$q)$_4$]·DMF **1-DMF(Ho)**, FTIR ν (cm−1): 1682 (s), 1550 (s), 1485 (s), 1450 (s), 1390 (s), 1373 (s), 1358 (m), 1250 (w), 1215 (w), 1138 (w), 1107 (m), 1051 (w), 936 (m), 875 (w), 858 (m), 810 (m), 787 (m), 742 (s), 684 (w), 667 (m). Elem. Anal. for C$_{39}$H$_{23}$Br$_8$N$_5$O$_5$HoNa; C = 31.9%, N = 4.8%, H = 1.6%; found C = 31.5%, N = 4.8%, H = 1.6%. Elemental ratio estimated by electron probe microanalysis (EPMA): (Exp) Teo Dy : Na : Br = (0.99)1 : (0.98)1 : (8.01)8. TG measurement shows a similar thermal behavior than for **1-DMF(Dy)**.

Na[Dy(5,7-ClIq)$_4$]·DMF **2-DMF(Dy)**, FTIR ν (cm^{-1}): 1677 (s), 1567(w), 1543 (s), 1482 (s), 1437 (s), 1387 (s), 1372 (s), 1355 (m), 1245 (w), 1217 (w), 1133 (w), 1105 (m), 1046 (w), 954 (m), 872 (w), 846 (m), 809 (m), 786 (m), 742 (s), 699 (m), 662 (m). Elem. Anal. for C$_{39}$H$_{23}$Cl$_4$I$_4$N$_5$O$_5$DyNa; C = 31.7%; N = 4.7%; H = 1.6%; found C = 31.8%, N = 4.8%, H = 1.7%. Elemental ratio estimated by electron probe microanalysis (EPMA): (Exp) Teo Dy : Na : Cl : I = (1.02)1 : (1.01)1 : (3.97)4 : (4.02)4. TG measurement shows mass losses at 280 °C, 520°C and continuing the mass loss until 900°C.

Na[Tb(5,7-ClIq)$_4$]·DMF **2-DMF(Tb)**, FTIR ν (cm^{-1}): 1677 (s), 1566(w), 1543 (s), 1482 (s), 1437 (s), 1387 (s), 1372 (s), 1355 (m), 1245 (w), 1217 (w), 1133 (w), 1105 (m), 1046 (w), 954 (m), 872 (w), 846 (m), 809 (m), 786 (m), 742 (s), 699 (m), 662 (m). Elem. Anal. for C$_{39}$H$_{23}$Cl$_4$I$_4$N$_5$O$_5$TbNa; C = 31.7%; N = 4.7%; H = 1.6%; found C = 31.8%, N = 4.8%, H = 1.7%. Elemental ratio estimated by electron probe microanalysis (EPMA): (Exp) Teo Tb : Na : Cl : I = (1.01)1 : (0.99)1 : (3.98)4 : (4.00)4. Thermogravimetric analysis shows a similar behavior compared with compound **2-DMF(Dy)**.

Na[Er(5,7-ClIq)$_4$]·DMF **2-DMF(Er)**, FTIR ν (cm^{-1}): 1677 (s), 1562(w), 1543 (s), 1482 (s), 1437 (s), 1387 (s), 1372 (s), 1355 (m), 1245 (w), 1217 (w), 1133 (w), 1105 (m), 1046 (w), 954 (m), 872 (w), 846 (m), 809 (m), 786 (m), 742 (s), 699 (m), 662 (m). Elem. Anal. for C$_{39}$H$_{23}$Cl$_4$I$_4$N$_5$O$_5$ErNa; C = 31.6%; N = 4.7%; H = 1.6%; found C = 31.6%, N = 4.8%, H = 1.5%. Elemental ratio estimated by electron probe microanalysis (EPMA): (Exp) Teo Dy : Na : Cl : I = (1.03)1 : (1.01)1 : (3.96)4 : (3.97)4. Thermogravimetric analysis shows a similar behavior compared with compound **2-DMF(Dy)**.

Na[Ho(5,7-ClIq)$_4$]·DMF **2-DMF(Ho)**, FTIR ν (cm^{-1}): 1677 (s), 1567(w), 1543 (s), 1482 (s), 1437 (s), 1387 (s), 1372 (s), 1357 (m), 1245 (w), 1219 (w), 1133 (w), 1105 (m), 1046 (w), 954 (m), 872 (w), 848 (m), 809 (m), 786 (m), 744 (s), 699 (m), 662 (m). Elem. Anal. for C$_{39}$H$_{23}$Cl$_4$I$_4$N$_5$O$_5$HoNa; C = 31.7%; N = 4.7%; H = 1.6%; found C = 31.8%, N = 4.7%, H = 1.5%. Elemental ratio estimated by electron probe microanalysis (EPMA): (Exp) Teo Dy : Na : Cl : I = (1.00)1 : (1.03)1 : (3.97)4 : (3.98)4. Thermogravimetric analysis shows a similar behavior compared with compound **2-DMF(Dy)**.
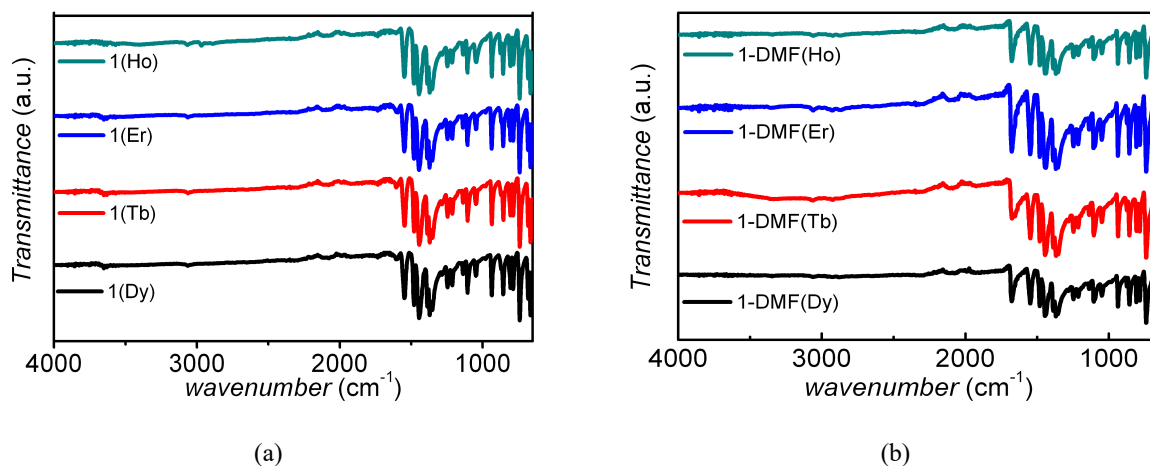
S.1.4. Infrared spectroscopy

(a)

(b)

Figure S1. Infrared Spectra of (a) compounds Na[Ln(5,7-Br$_2$q)$_4$] (**1(Dy)**; **1(Tb)**; **1(Er)**; **1(Ho)**); (b) compounds Na[Ln(5,7-Br$_2$q)$_4$]·DMF (**1-DMF(Dy)**; **1-DMF(Tb)**; **1-DMF(Er)**; **1-DMF(Ho)**)
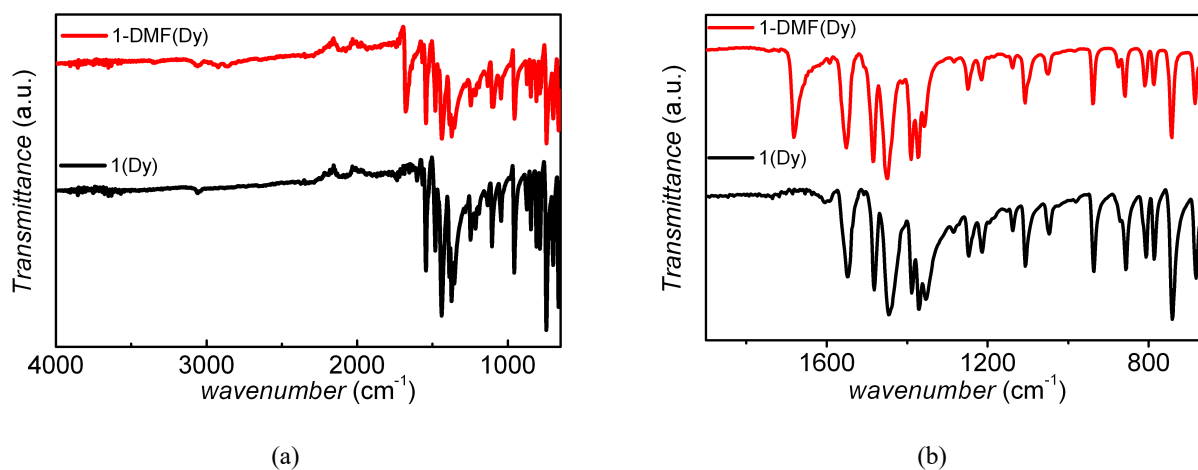

(a)

(b)

Figure S2. (a) Comparison between the raw material of Na[Dy(5,7-Br$_2$q)$_4$] **1(Dy)** and the recrystallized material Na[Dy(5,7-Br$_2$q)$_4$]·DMF **1-DMF(Dy)**. Both material present the same IR bands, with the exception of the signal around 1650 cm^{-1} of the DMF molecule. (b) A zoom of the region 700–1900 cm^{-1} is shown.
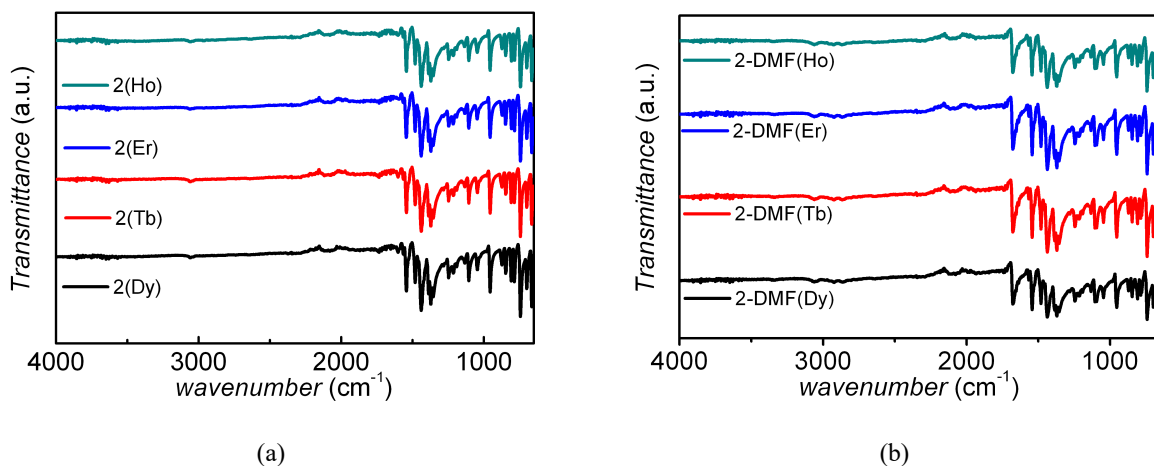
Figure S3. Infrared Spectra of (a) compounds Na[Ln(5,7-ClIq)$_4$] **2(Dy)**; **2(Tb)**; **2(Er)**; **2(Ho).** (b) compounds Na[Ln(5,7-ClIq)$_4$]·DMF **2-DMF(Dy)**; **2-DMF(Tb)**; **2-DMF(Er)**; **2-DMF(Ho)**.

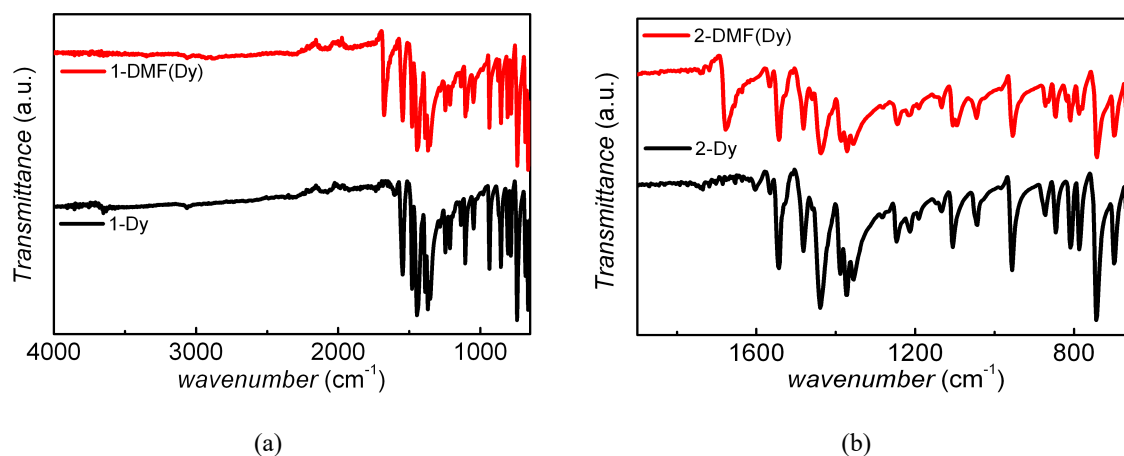**Figure S4.** (a) Comparison between the raw material of Na[Ln(5,7-ClIq)$_4$] **2(Dy)** and the recrystallized material Na[Ln(5,7-ClIq)$_4$]·DMF **2-DMF(Dy)**. Both material present the same IR bands, with the exception of the signal around 1650 cm^{-1} of the DMF molecule. (b) A zoom of the region 700–1900 cm^{-1} is shown.
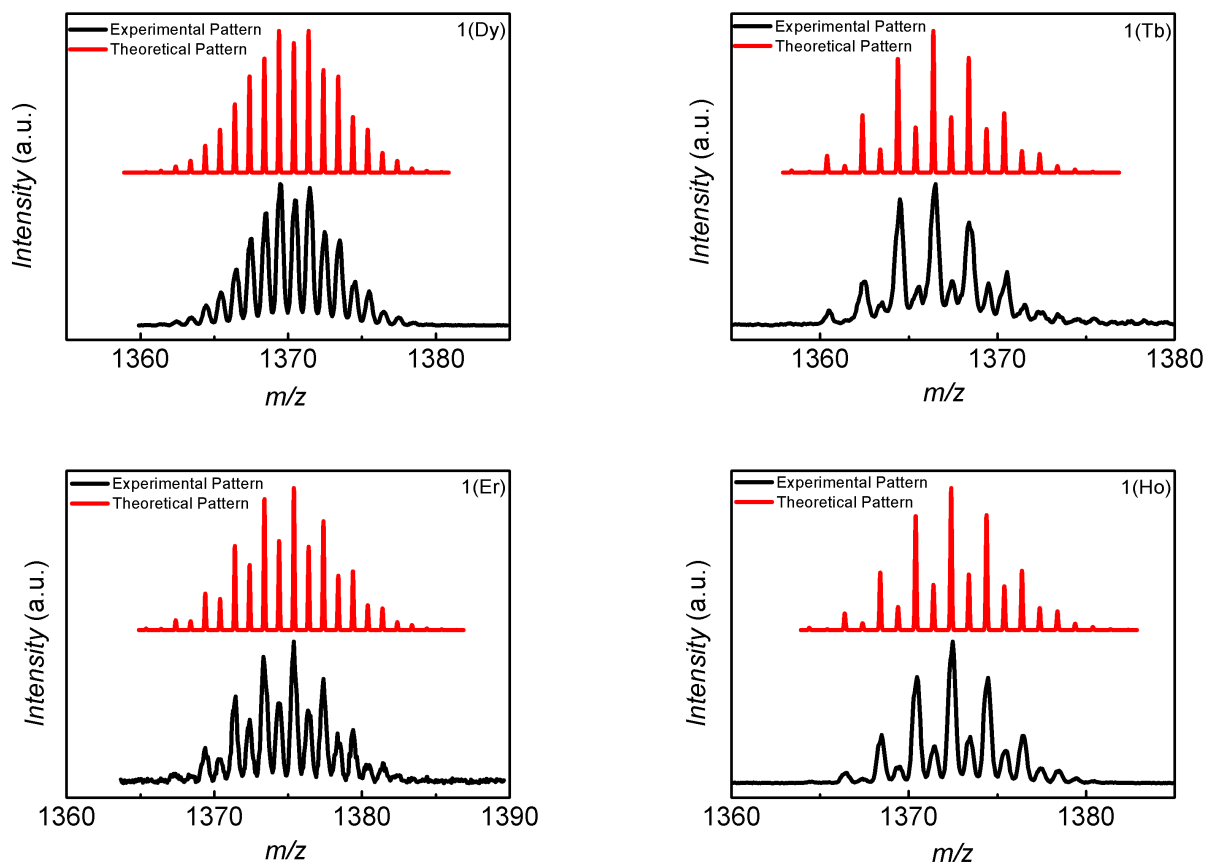
Figure S5. ES-MS spectrums in the negative mode detecting the $[Ln(5,7-Br_2q)_4]^-$ anion of the synthesized $Na[Ln(5,7-Br_2q)_4]$ complexes (**1(Dy)**, **1(Tb)**, **1(Er)** and **1(Ho)**).

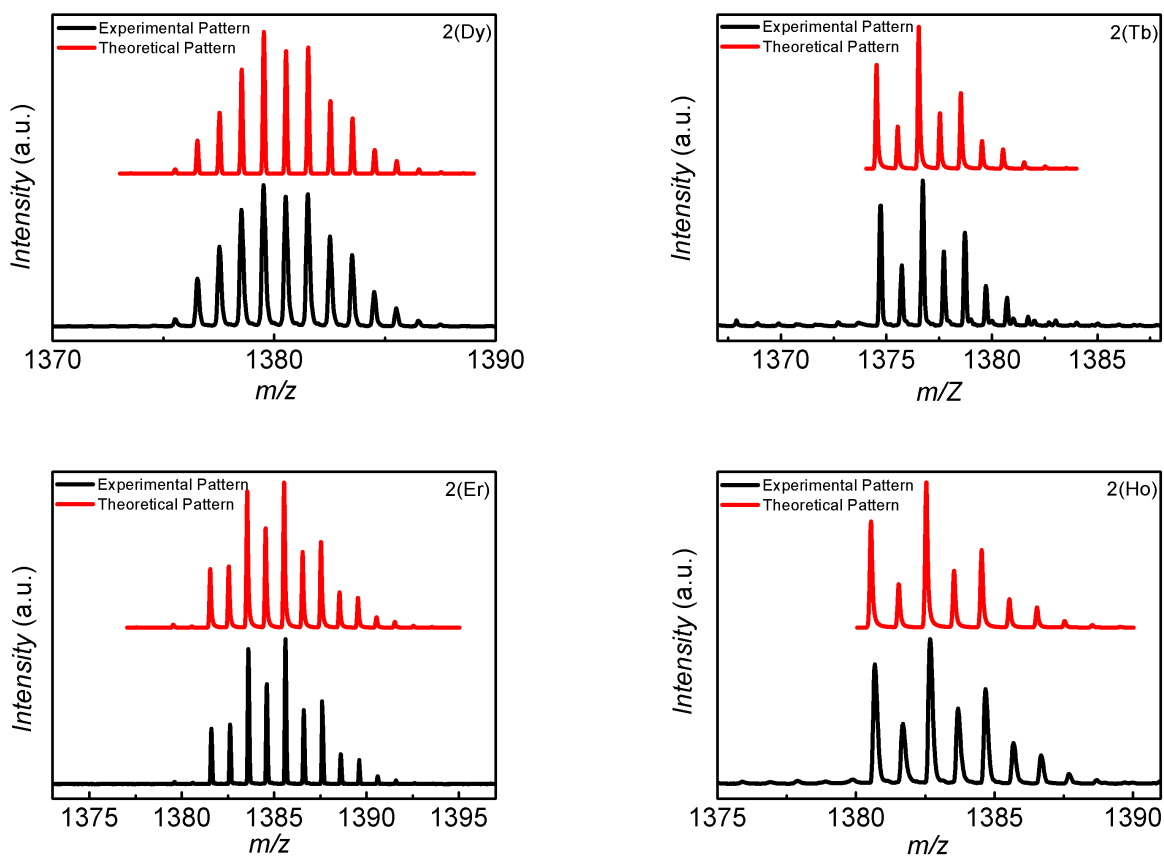**Figure S6.** ES-MS spectrums in the negative mode match perfectly with the theoretical pattern of [Ln(5,7-ClIq)$_4$]$^-$ anion of the synthesized Na[Ln(5,7-ClIq)$_4$] complexes, **2(Dy)**, **2(Tb)**, **2(Er)**, **2(Ho).**

A 20% weight loss at 220°C is observed for the complexes Na[Ln(5,7-Br$_2$q)$_4$] which correspond to the loss of one 5,7-Br$_2$q ligand plus a Na$^+$. For the complexes Na[Ln(5,7-ClIq)$_4$] it is possible to determine that also these systems lost one ligand plus a Na$^+$, but in this case the mass loss occurs at a higher temperature (340°C). The shapes of the curves of both compounds are different; for the complexes with the 5,7ClIq, an almost vertical drop of the mass loss is observed. The thermal behavior of the Na[Ln(5,7-Br$_2$q)$_4$] complexes is completely different from the Na[Ln(5,7-ClIq)$_4$], which are more thermally stable than the Na[Ln(5,7-Br$_2$q)$_4$] compounds. Also, for the recrystallized material, it is also possible to determine that the complexes with the 5,7-ClIq ligand are more stable (approx. 30°C) than the systems with the 5,7-Br$_2$q ligands.

For the recrystallized compounds with DMF, it is possible to observe that for the complexes with the 5,7Br$_2$q ligand a weight loss of 5 % is observed that corresponds to the loss of the DMF molecule, and the subsequent weight loss correspond also to the thermal decomposition of one ligand and a Na$^+$ atom.

Summarizing, the thermal behavior observed for these compounds shows that the more stable complexes are those with the 5,7-ClIq ligand (up to 340°C). The 5,7-Br$_2$q complexes are less stable with a decomposing temperature of 220°C in accordance with the thermal properties of other 5,7-dihaloquinolinate lanthanide complexes reported previously[6] (Figure S7). In addition, it is observed that the recrystallized complexes are less stable than the microcrystalline and the amorphous materials (Figure S7).
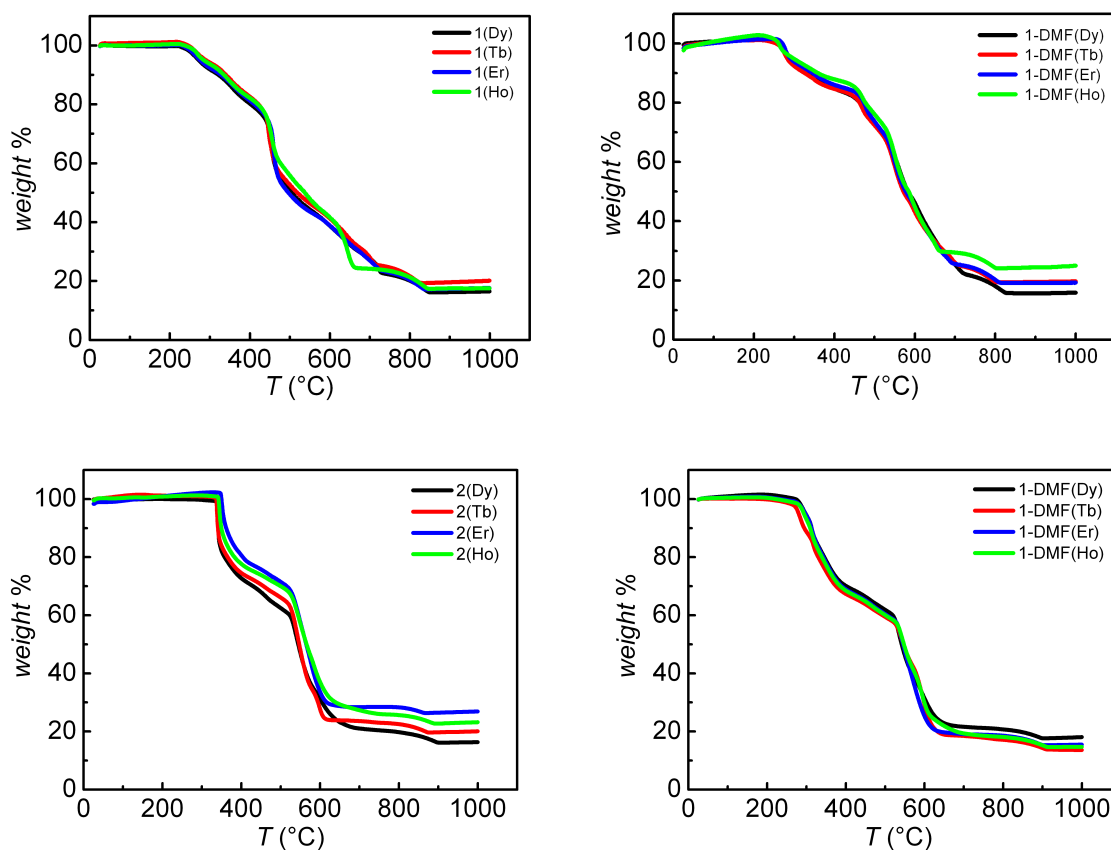

Figure S7. TG measurements of the complexes of formula Na[Dy(5,7-X$_2$q)$_4$] (**1** and **2**) and Na[Dy(5,7-X$_2$q)$_4$]·DMF (**1-DMF** and **2-DMF**), where   X = Br, Cl-I.

S.2. SINGLE CRYSTAL X-RAY DIFFRACTION

S.2.1. Experimental details

Single crystals of compounds **1-DMF(Dy)**; **1-DMF(Tb)**; **1-DMF(Er)**; **1-DMF(Ho)**; **2-DMF(Dy)**; **2-DMF(Tb)**; **2-DMF(Er)**; **2-DMF(Ho)** were mounted on glass fibers using a viscous hydrocarbon oil to coat the crystal and then transferred directly to the cold nitrogen stream for data collection. X-ray data were collected at 120 K on a Supernova diffractometer equipped with a graphite-monochromated Enhance (Mo) X-ray Source ($\lambda = 0.71073$ Å). The program CrysAlisPro, Oxford Diffraction Ltd., was used for unit cell determinations and data reduction. Crystal structures were solved and refined against all F^2 values using the SHELXTL suite of programs[4,5]. Non-hydrogen atoms were refined anisotropically and hydrogen atoms were placed in calculated positions that were refined using idealized geometries (riding model). A summary of the data collection and structure refinements is provided in Tables S1 and S2. CCDC-1562344 to -1562351 contain the supplementary crystallographic data for this paper. These data can be obtained free of charge from The Cambridge Crystallographic Data Centre via www.ccdc.cam.ac.uk/data_request/cif.

Table S1: Crystallography data for compounds $Na[Ln(5,7-Br_2q)_4]\cdot DMF$ (**1-DMF**)

	1-DMF(Dy)	**1-DMF(Er)**	**1-DMF(Ho)**	**1-DMF(Tb)**
Empirical formula	$C_{39}H_{23}Br_8DyN_5NaO_5$	$C_{39}H_{23}Br_8ErN_5NaO_5$	$C_{39}H_{16}Br_8HoN_5NaO_5$	$C_{39}H_{23}Br_8N_5NaO_5Tb$
Formula weight	1466.39	1471.15	1461.77	1462.81
Temperature/K	120.15	120.00(10)	120.00(10)	120.00(10)
Crystal system	monoclinic	monoclinic	monoclinic	monoclinic
Space group	$P2_1/c$	$P2_1/c$	$P2_1/c$	$P2_1/c$
a/Å	10.15000(10)	10.102(2)	10.141(2)	10.134(2)
b/Å	20.7270(2)	20.815(4)	20.736(4)	20.725(4)
c/Å	20.3813(3)	20.388(4)	20.365(4)	20.432(4)
α/°	90	90	90	90
β/°	92.0990(10)	91.50(3)	92.05(3)	92.00(3)
γ/°	90	90	90	90
Volume/Å³	4284.92(9)	4285.6(15)	4279.6(15)	4288.6(15)
Z	4	4	4	4
ρ_{calc}g/cm³	2.273	2.28	2.269	2.266
μ/mm⁻¹	9.264	9.477	9.378	9.163
F(000)	2756	2764	2732	2752
Crystal size/mm³	0.05 × 0.04 × 0.03	0.1 × 0.06 × 0.05	0.06 × 0.03 × 0.03	0.05 × 0.04 × 0.03
Radiation	MoKα ($\lambda = 0.71073$)	MoKα ($\lambda = 0.71073$)	MoKα ($\lambda = 0.71073$)	MoKα ($\lambda = 0.71073$)
2Θ range for data collection/°	5.608 to 50.074	5.754 to 55.042	5.774 to 55.018	5.764 to 55.088
Reflections collected	56744	171633	107999	183027
Independent reflections	7569 [R_{int} = 0.0649, R_{sigma} = 0.0414]	9830 [R_{int} = 0.1386, R_{sigma} = 0.0486]	9793 [R_{int} = 0.0947, R_{sigma} = 0.0517]	9850 [R_{int} = 0.0970, R_{sigma} = 0.0376]
Data/restraints/ parameters	7569/0/524	9830/0/519	9793/0/534	9850/0/524
Goodness-of-fit on F^2	1.054	1.024	1.038	1.04
Final R indexes [I>=2σ (I)]	R_1 = 0.0436, wR_2 = 0.0942	R_1 = 0.0540, wR_2 = 0.1188	R_1 = 0.0431, wR_2 = 0.0880	R_1 = 0.0492, wR_2 = 0.1134
Final R indexes [all data]	R_1 = 0.0583, wR_2 = 0.1011	R_1 = 0.0788, wR_2 = 0.1310	R_1 = 0.0686, wR_2 = 0.0984	R_1 = 0.0687, wR_2 = 0.1246
Largest diff. peak/hole/ e Å⁻³	3.41/-0.90	4.60/-1.84	2.51/-1.14	3.91/-1.51

Table S2: Crystallography data for compounds Na[Ln(5,7-ClIq)$_4$]·DMF (**2-DM**

	2-DMF(Dy)	2-DMF(Er)	2-DMF(Ho)	1-DMF(Tb)
Empirical formula	$C_{39}H_{23}Cl_4DyI_4N_5NaO_5$	$C_{39}H_{23}Cl_4ErI_4N_5NaO_5$	$C_{39}H_{23}Cl_4HoI_4N_5NaO_5$	$C_{39}H_{23}Cl_4I_4N_5NaO_5Tb$
Formula weight	1476.51	1481.27	1478.94	1472.93
Temperature/K	119.95(10)	122(3)	120.2(2)	120.00(10)
Crystal system	monoclinic	monoclinic	monoclinic	monoclinic
Space group	P2$_1$/c	P2$_1$/c	P2$_1$/c	P2$_1$/c
a/Å	10.3511(2)	10.3130(2)	10.3286(2)	10.3418(2)
b/Å	23.6016(3)	23.5492(3)	23.5723(5)	23.5877(4)
c/Å	18.0564(3)	18.0869(4)	18.0707(4)	18.0041(4)
α/°	90	90	90	90
β/°	94.8120(10)	94.440(2)	94.611(2)	94.913(2)
γ/°	90	90	90	90
Volume/Å^3	4395.68(13)	4379.45(14)	4385.41(16)	4375.77(15)
Z	4	4	4	4
ρ_{calc}g/cm^3	2.231	2.247	2.24	2.236
μ/mm^{-1}	4.811	5.039	4.923	4.742
F(000)	2756	2764	2760	2752
Crystal size/mm^3	0.03 × 0.03 × 0.02	0.1 × 0.07 × 0.05	0.1 × 0.07 × 0.05	0.15 × 0.14 × 0.12
Radiation	MoKα (λ = 0.71073)	MoKα (λ = 0.71073)	MoKα (λ = 0.71073)	MoKα (λ = 0.71073)
2Θ range for data collection/°	5.652 to 50.054	6.472 to 55.854	6.524 to 61.016	6.718 to 56.128
Reflections collected	107609	36003	130392	19111
Independent reflections	7761 [R$_{int}$ = 0.1123, R$_{sigma}$ = 0.0492]	9276 [R$_{int}$ = 0.0626, R$_{sigma}$ = 0.0740]	13390 [R$_{int}$ = 0.1364, R$_{sigma}$ = 0.0760]	8858 [R$_{int}$ = 0.0481, R$_{sigma}$ = 0.0832]
Data/restraints/ parameters	7761/0/534	9276/0/529	13390/0/534	8858/0/534
Goodness-of-fit on F^2	1.063	1.078	1.04	1.065
Final R indexes [I>=2σ (I)]	R$_1$ = 0.0330, wR$_2$ = 0.0590	R$_1$ = 0.0412, wR$_2$ = 0.0595	R$_1$ = 0.0428, wR$_2$ = 0.0649	R$_1$ = 0.0456, wR$_2$ = 0.0786
Final R indexes [all data]	R$_1$ = 0.0521, wR$_2$ = 0.0662	R$_1$ = 0.0727, wR$_2$ = 0.0728	R$_1$ = 0.0869, wR$_2$ = 0.0804	R$_1$ = 0.0756, wR$_2$ = 0.0947
Largest diff. peak/hole/ e Å^{-3}	0.76/-0.86	1.00/-1.21	1.65/-1.28	1.20/-1.20

Response to B-Alerts. B-Level Alerts for 1-DMF(Dy), 1-DMF(Er) and 1-DMF(Tb). This alert B is related to the isotropic refinement of the C23 and C43 of the structure. This is the result of a minor structural disorder in which the quinolinate ligand is inverted, causing the Br28 (or Br48) atom to lie on top of C23. This disorder, of a magnitude < 5%, is only evident for the bulkier atom (Br), and despite all efforts to model it, it provided no improvement on the structural model. For 2-DMF(Er), the B alert is related to C39 and anisotropic refinement gives a non-realistic ellipsoid, so was keep isotropic

S.2.2. Structural description of Na[Ln(5,7-Br$_2$q)$_4$]·DMF (1-DMF)

The X-ray structure of the complexes, where Ln = Dy[III], Tb[III], Er[III], Ho[III], are isostructural crystallizing in a monoclinic P2$_{1/C}$ space group (Table S1). The recrystallization on DMF (omitted in the figure) causes that one solvent molecule is coordinated to the Na$^+$ and this cation is linked through oxygen atoms to the anionic complex, [Ln(5,7-Br$_2$q)$_4$]$^-$ (Figure S8). In order to describe the geometry of the Ln complexes, continuous shape measurement (CShM´s) calculations were done using the SHAPE code [7,8]. The calculations shows that the geometry of the Ln complexes can be almost equally described as distorted bicapped trigonal prism (btp), square antiprism (sa) and triangular dodecahedron (td). The distortion path was also calculated between these three ideal geometries (btp to sa; btp to td and sa to td), but the value of CShM´s of the experimental structures does not follow any of the paths between the ideal geometries. This indicates the highly distorted geometry that these complexes do possess (Figure S10).

The metal-metal distances between the closest lanthanides, centers are 10.3021(5) Å, 10.3249(5) Å, 10.2985(5) Å and 10.2932(4) Å, for the **1-DMF(Dy)**, **1-DMF(Tb)**, **1-DMF(Er)** and **1-DMF(Ho)** complexes, respectively. The crystal lattice of these compounds are also stabilized by the existence of π- π stacking between the aromatic rings of the quinolinolates ligands, the distances of these π- π interactions are 3.323 and 3.301 Å for **1-DMF(Dy)**, 3.315 and 3.298 Å for **1-DMF(Tb)**, 3.323 and 3.289 Å for **1-DMF(Er)**, and finally for **1-DMF(Ho)** the distance are 3.315 and 3.290 Å (Figure S8). The crystal lattices of these systems are stabilized by the existence of hydrogen bonds between bromide or oxygen atoms, and hydrogen atoms of the ligands and the solvent molecule. Moreover, halogen bonds in these structures between the bromide atoms and the aromatic carbon atoms contribute to the stabilization of the crystal lattice: B46-C13; Br26-C32; Br16-C27; Br16-C28 (Tables S3 – S5).
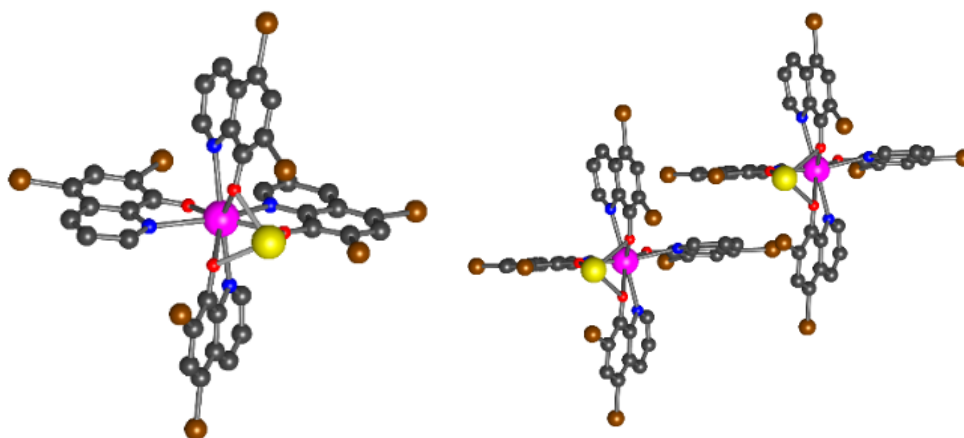

Figure S8. X-ray structure of **1-DMF(Dy)** Na[Dy(5,7-Br2q)4]·DMF (left), DMF molecule omitted. π- π interactions between the aromatic rings of two ligands of two different complexes (right). Dysprosium: pink; sodium: yellow; carbon: black; oxygen: red; nitrogen: blue; bromide: brown.

S.2.3. Structural description of Na[Ln(5,7-ClIq)$_4$]·DMF (2-DMF)

X-ray crystallography shows that all these complexes as well as the Na[Ln(5,7-Br2q)4]·DMF systems crystallized in a monoclinic P21/C space group (Table S2). As in the previous complex, the Na+ and this cation is linked through oxygen atoms to the [Ln(5,7-ClIq)4]- (Figure S9). The SHAPE calculations reflect that the Ln complexes also present distorted geometries, which are close to a distorted bicapped trigonal prism (btp), square antiprism (sa) or triangular dodecahedron (td). In addition, the values of CShM´s of the experimental structures do not follow any of the paths between the ideal geometries. This shows the highly distorted geometry of the complexes (Figure S10).

The metal distances between nearest lanthanides are 9.3008(4) Å, 9.2795(5) Å, 9.3049(5) Å and 9.3014(4) Å, for the **2-DMF(Dy)**, **2-DMF(Tb)**, **2-DMF(Er)** and **2-DMF(Ho)** complexes, respectively. The crystal lattice of these compounds are stabilized by the existence of π- π stacking between the aromatic rings of the quinolinates ligands, by hydrogen bonds and also by halogen bonds 37. The distances of the π-π interactions are 3.304 Å for **2-DMF-Dy**, 3.313 Å for **2-DMF(Tb)**, 3.295 Å for **2-DMF(Er)**, and 3.292 Å for **2-DMF(Ho)**. One of the halogen bonds is between the Cl atom of one complex with the I atom of the nearest Ln complex (I48-Cl36), with distances of 3.694(2) Å for **2-DMF(Dy)**, 3.679(2) Å for **2-DMF(Tb)**, 3.705(2) Å for **2-DMF(Er)**, and 3.700(1) Å for **2-DMF(Ho)**. (Figure S9). Other types of halogen bonds between iodine or chlorines and carbon atoms of the aromatic rings of the ligands are observed as well; I38-C25; Cl46-C35; Cl46-C40. (Tables S3 – S5).
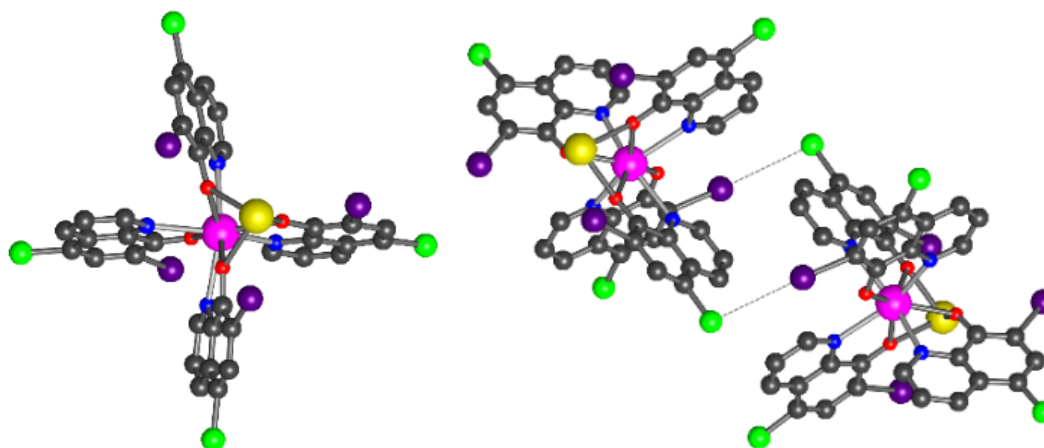
Figure S9. X-ray structure of the **2-DMF(Dy)** Na[Dy(5,7-ClIq)4]·DMF (left), DMF molecule omitted. Halogen bond interactions between the complexes (right). Dysprosium: pink; sodium: yellow; carbon: black; oxygen: red; nitrogen: blue; chlorine: green; iodine: purple.

S.2.4. Summary of intermolecular interactions

Table S3: Selected distances of halogen bonds networks of the complexes Na[Ln(5,7-Br$_2$q)$_4$]·DMF (**1-DMF**) and Na[Ln(5,7-ClIq)$_4$]·DMF (**2-DMF**).

Na[Ln(5,7-Br$_2$q)$_4$]·DMF	Br46-C13 (Å)	Br26-C32 (Å)	Br16-C27 (Å)	Br16-C28 (Å)
1-DMF(Dy)	3.390	3.519	3.470	3.425
1-DMF(Tb)	3.398	3.510	3.468	3.426
1-DMF(Er)	3.378	3.531	3.454	3.430
1-DMF(Ho)	3.393	3.519	3.464	3.414
Na[Ln(5,7-ClIq)$_4$]·DMF	I48-Cl36 (Å)	Cl46-C35 (Å)	Cl46-C40 (Å)	I38-C25 (Å)
2-DMF(Dy)	3.694	3.398	3.224	3.665
2-DMF(Tb)	3.679	3.391	3.229	3.653
2-DMF(Er)	3.705	3.383	3.212	3.642
2-DMF(Ho)	3.700	3.388	3.229	3.649

Table S4: Selected angles of C-X(halogen)----D of the complexes Na[Ln(5,7-Br$_2$q)$_4$]·DMF (**1-DMF**) and Na[Ln(5,7-ClIq)$_4$]·DMF (**2-DMF**).

Na[Ln(5,7-Br$_2$q)$_4$]·DMF	C46Br46C13 (°)	C26Br26C32 (°)	C16Br16C27 (°)	C16Br16C28 (°)
1-DMF(Dy)	154.35	131.96	145.87	129.85
1-DMF(Tb)	153.88	131.84	145.80	129.95
1-DMF(Er)	156.35	131.88	144.92	128.81
1-DMF(Ho)	154.71	131.33	145.83	129.88
Na[Ln(5,7-ClIq)$_4$]·DMF	C48I48Cl36 (°)	C46Cl46C35 (°)	C46Cl46C40 (°)	C38I38C25 (°)
2-DMF(Dy)	164.84	154.27	152.63	118.70
2-DMF(Tb)	164.95	153.34	152.36	118.81
2-DMF(Er)	163.61	155.03	153.40	118.53
2-DMF(Ho)	164.03	155.13	153.28	118.60

Table S5: Distances of hydrogen bonds network of the two families of complexes, Na[Ln(5,7-Br$_2$q)$_4$]·DMF (**1-DMF**) and Na[Ln(5,7-ClIq)$_4$]·DMF (**2-DMF**). Labels with X' are referred to the closest molecules.

Na[Ln(5,7-Br$_2$q)$_4$]·DMF	H24-Br16' and Br16-H24' (Å)	H34-Br48' and Br48-H34'(Å)	H10E-Br36' and Br36-H10E' (Å)	H10D-Br18' and Br18-H10D' (Å)	H13-O101' and O101-H13'(Å)
1-DMF(Dy)	2.859	3.035	2.947	3.045	2.627
1-DMF(Tb)	2.873	3.056	2.976	3.063	2.658
1-DMF(Er)	2.896	3.058	2.935	3.069	2.661
1-DMF(Ho)	2.889	3.038	2.952	3.036	2.645
Na[Ln(5,7-ClIq)$_4$]·DMF	H33-Cl46' and Cl46-H33' (Å)				
2-DMF(Dy)	2.799				
2-DMF(Tb)	2.780				
2-DMF(Er)	2.801				
2-DMF(Ho)	2.803				

S.2.5. SHAPE analysis

The molecular structure of these compounds, (**1-DMF**) and (**2-DMF**) have been described with the SHAPE code, indicating that complexes have distorted geometries closest to three different geometries (bicapped trigonal prism; square antiprism and triangular dodecahedron). The value of CShM´s of the experimental structures does not follow any of the paths between the ideal geometries indicating the highly distorted geometry that these complexes have.

The geometries that these systems present are not unusual since most Ln complexes present distorted forms of square antiprism, triangular dodecahedron or bicapped trigonal prism geometries[9–13]. The metal centers of a trinuclear dysprosium quinolinato reported previously by Chilton et al.[14] present similar geometries as the ones presented in this work. Our group has recently reported elsewhere a similar compounds, of formula Na[Ln(5,7-Cl$_2$q)$_4$]·DMF, where Ln = Dy[III], in which the lanthanides centers present a similarly distorted geometry[15].

As described in the X-ray results section, the existence of several intermolecular interactions, like hydrogen bonds, π- π stacking interactions and halogen bonds stabilized the crystal lattice of these systems (lanthanide complexes). Several examples exist in the literature, in which the first two kinds of interactions, one or combined, stabilized the crystalline lattice[10,16–23]. The halogen bond interactions have been less reported, but some works have established the necessary considerations to evaluate a halogen bond and according to this, the families Na[Ln(5,7-Cl$_2$q)$_4$]·DMF, present halogen bonds of the type; I-Cl, Cl-C(aromatic), Br-C(aromatic) and I-C(aromatic)[24,25]. Between the two families of compounds the compounds with 5,7-Br$_2$q ligands present a higher number of hydrogen bonds, and extra π- π stacking interaction, than the complexes with the 5,7-ClIq ligands. For both families halogen bonds with the other types of intermolecular interactions confers the necessary stability for these compounds to crystallize.
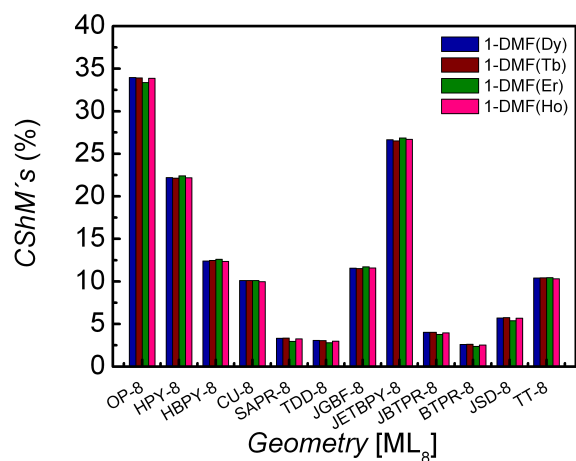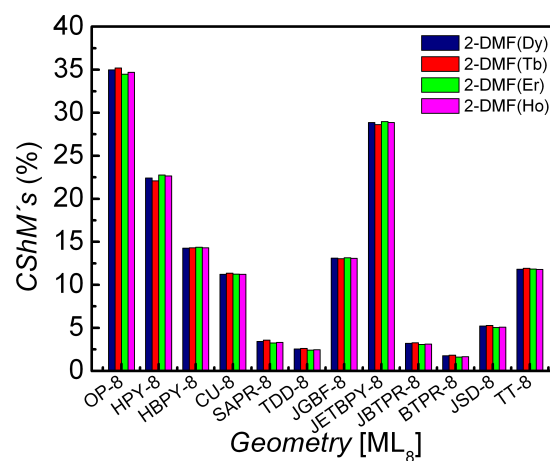
(a)   (b)

Figure S10. Results of the SHAPE measurements for (a) the Na[Ln(5,7-Br$_2$q)$_4$]·DMF (**1-DMF**) complexes and (b) the Na[Ln(5,7-ClIq)$_4$]·DMF (**2-DMF**) complexes

S.3. X-RAY POWDER DIFFRACTION

Amorphous, polycrystalline or crystalline samples of all compounds were lightly ground with a pestle in an agate mortar and filled into 0.5 mm borosilicate capillaries prior to being mounted and aligned on a Empyrean PANalytical powder diffractometer, using Cu Kα radiation (λ = 1.54056 Å). For each sample, two or three repeated measurements were collected at room temperature (2θ = 2 – 40°) and merged into a single diffractogram.

XRPD analysis of complexes of both families were done to the products directly obtained from the synthesis in EtOH. The XPD pattern of Na[Ln(5,7-Br$_2$q)$_4$] **(1)**, is quite similar for all the Ln complexes, but some differences exist that are due to the existence of amorphous material. For the complexes of the family, Na[Ln(5,7-ClIq)$_4$] **(2)** the XRPD diffractogram reveals that the material is completely amorphous. The recrystallized products of Na[Ln(5,7-Br$_2$q)$_4$]·DMF and Na[Ln(5,7-ClIq)$_4$]·DMF are isostructural and also are in agreement with their simulated patterns (Figure S11 – S12), which demonstrates that the crystal structures of compounds **(1-DMF)** and **(2-DMF)** are truly representative of the bulk materials. In addition, **2-DMF** materials are more amorphous than **1-DMF**. The differences in intensity are due to the preferred orientation of the powder samples.

(a)   (b)
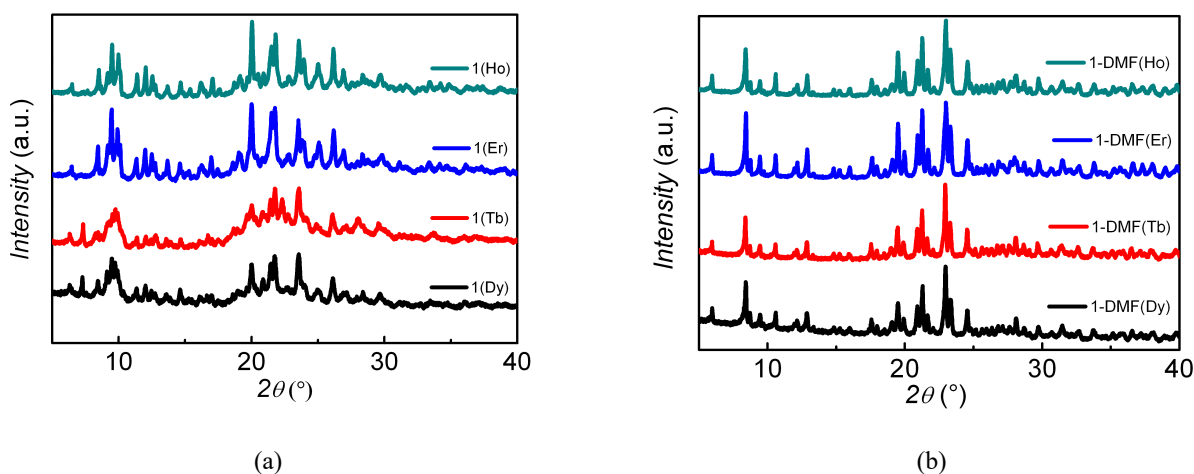
Figure S11. PXRD patterns of the different crystalline phases of the compounds Na[Ln(5,7-Br$_2$q)$_4$] **(1)** (a) and Na[Ln(5,7-Br$_2$q)$_4$]·DMF **(1-DMF)** (b).

(a)   (b)
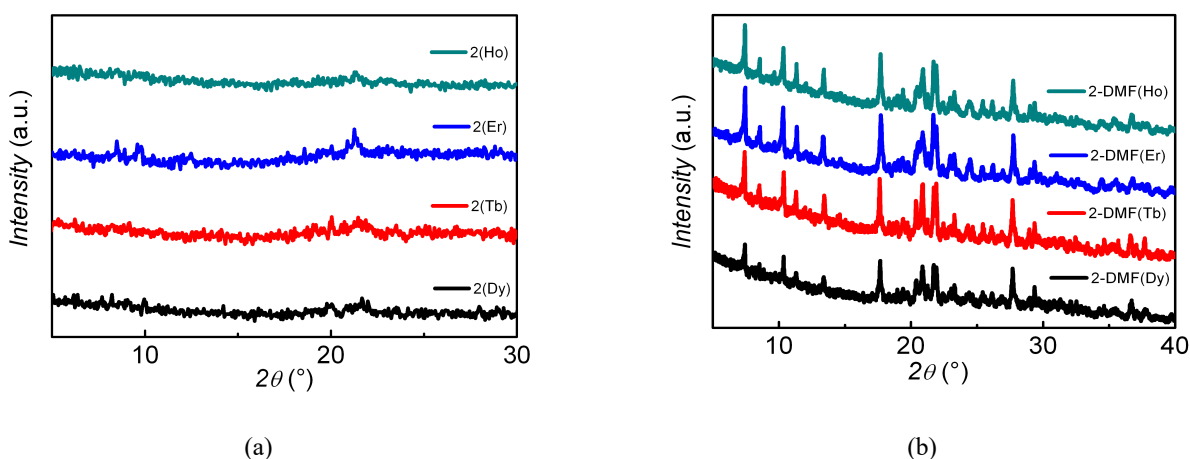
Figure S12. PXRD patterns of the different crystalline phases of the compounds Na[Ln(5,7-ClIq)$_4$] **(2)** (a) and Na[Ln(5,7-ClIq)$_4$]·DMF **(2-DMF)** (b).
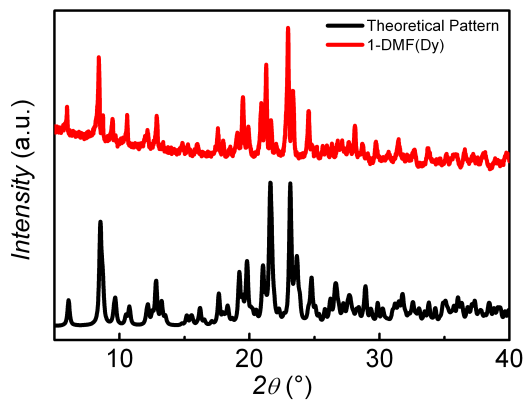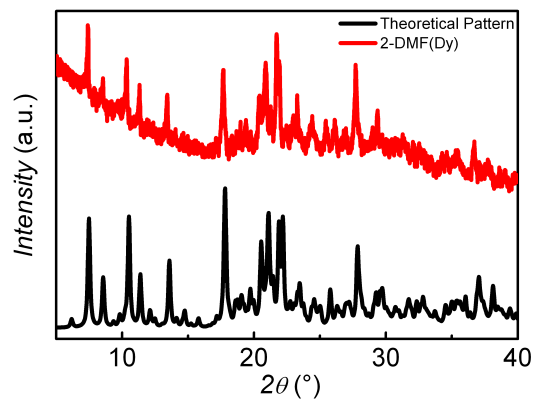
(a)   (b)

Figure S13. PXRD patterns of the different crystalline phases of the compounds, Na[Dy(5,7-Br$_2$q)$_4$·DMF (a) and Na[Dy(5,7-ClIq)$_4$]·DMF (b). In black, the theoretical patterns of the compounds crystallized in DMF.

S.4. MAGNETIC SUSCEPTIBILITY MEASUREMENTS

Magnetic measurements were performed on ground crystals of the different compounds in a Quantum Design Physical Property Measurement System (PPMS). Variable-temperature (2 - 300 K) direct current (dc) magnetic susceptibility measurements were carried out under an applied field of 1000 G, and variable field magnetization measurements up to 5 T were performed at 2.0 K for all compounds. Variable-temperature (2 - 30 K) alternating current (ac) magnetic susceptibility measurements in a 3.9 G oscillating field at frequencies in the range of 10– 10000 Hz were carried out under a zero dc field for compounds **1-DMF(Dy)** and **2-DMF(Dy)**. The same measurements were repeated under different dc fields of 100 G, 300 G, 500 G and 700 G.

Additional ac susceptibility measurements at different frequencies with an applied dc field of 500G were done for compounds **1-DMF(Dy)** and **2-DMF(Dy)** in a Quantum Design MPMS XL-5 SQUID magnetometer. Finally, compounds **1-DMF(Tb)** and **2-DMF(Tb)** were measured under a dc field of 1500G at frequencies in the range of 1– 1000 Hz in the same SQUID magnetometer mention before.

S.4.1. Static magnetic susceptibility (dc)

Magnetic dc susceptibility measurements were carried out between 2 and 300 K at 1000 G for complexes **1-DMF(Dy)**; **1-DMF(Tb)**; **1-DMF(Er)**; **1-DMF(Ho)**; **2-DMF(Dy)**; **2-DMF(Tb)**; **2-DMF(Er)**; **2-DMF(Ho)**. The susceptibility values of all the complexes are in good agreement with the expected values for mononuclear complexes; Dy^{III} (S = 5/2, L =5, $^6H_{15/2}$, g = 4/3, $\chi_M T_{free-ion}$ = 14.17 emu K mol^{-1}), Tb^{III} (S =3, L =3, $^7F_6$, g = 3/2, $\chi_M T_{free-ion}$ = 11.81 emu K mol^{-1}), Er^{III} (S = 3/2, L =6, $^4I_{15/2}$, g = 36/5, $\chi_M T_{free\ ion}$ = 11.48 emu K mol^{-1}), and Ho^{III} (S =2, L =6, $^5I_8$, g = 5/4, $\chi_M T_{free\ ion}$ = 14.48 emu K mol^{-1})[16,26]. The $\chi_M T$ values decrease at low temperatures due to the thermal depopulation of the Stark sublevels and/or to the presence of intermolecular interactions (Figure 2). Magnetization measurements were done for all the compounds at 2K between 50 kG and -50 kG, in which only the dysprosium complexes clearly present butterfly magnetic hysteresis since these systems present fast Quantum Tunneling of Magnetization (QTM) under zero applied field with small or no remnant magnetization at zero field (Figure S14).
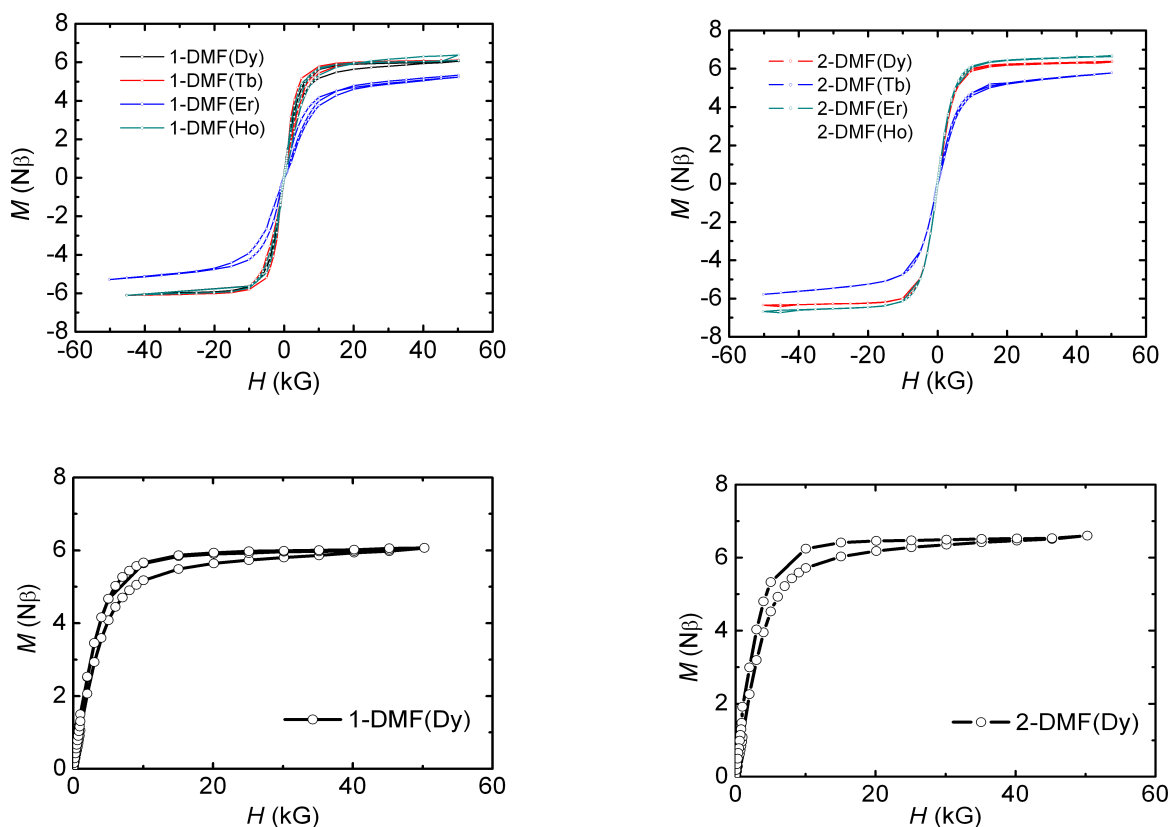

Figure S14. M(H) measurements between -50 kG to 50 kG for the recrystallized complexes of both families. Also, are presented the M(H) of the dysprosium complexes (**1-DMF(Dy)** and **2-DMF(Dy)**) showing the existence of hysteresis in these complexes.

S.4.2. Theoretical studies of the dc magnetic properties

In order to provide an approximated description of the ground multiplet energy levels and the magnetic properties of the reported compounds, we have applied the Radial Effective Charge (REC) model [27] using the SIMPRE computational package [28]. The energy level scheme of the compounds and the corresponding wave functions (Tables S6-S13) are obtained using the crystal structures of the compounds and the REC parameters D_r and Z_i, which correspond to the metal-to-ligand contraction and to the effective charge of the ligands, respectively. The D_r of the donor atoms have been calculated using the following empirical approximation[29] $D \approx \left(\frac{N_L}{V_M}\right) \cdot \frac{1}{E_M(E_L-E_M)}$; where N_L is the coordination number of the complex, V_M is the valence of the metal, and E_M and E_L are the Pauling electronegativities of the metal and the donor atom respectively. Such approximated relation has been obtained by fitting the phenomenological crystal field parameters of the families $CsNaYCl_6:Ln^{3+}$ and $CsNaYF_6:Ln^{3+}$, $LiYF_4:Ln^{3+}$ and $LaCl_3:Ln^{3+}$ using the REC model [30]. The obtained values of D_r (N) and D_r (O) for the Dy compounds are thus 1.20 Å and 0.98 Å. Note that this strategy leads to an approximation that allows us to restrict the number of free parameters to two, i.e. the effective charges of the nitrogen and oxygen atoms.

The initial effective charges were obtained by a two-parameter fit of the χT product of the analogous family of compounds $Na[Ln(5,7Cl_2q)_4]\cdot DMF$ measured under a magnetic field of 1000 G, obtaining Z_i (N) = 0.160 and Z_i (O) = 0.235 [15]. These parameters have also been able to reproduce the experimental χT product of **1-DMF(Dy)**; **1-DMF(Tb)**; **1-DMF(Er)**; **1-DMF(Ho)** with good agreement. On the other hand, in the second family (**2-DMF(Dy)**; **2-DMF(Tb)**; **2-DMF(Er)**; **2-DMF(Ho)**) a fit of the magnetic susceptibility was required to offer a more realistic description of the magnetic properties. In this case, the obtained parameters are Z_i (N) = 0.260 and Z_i (O) = 0.095. This lower effective charge in the oxygen donor atoms can be attributed to the presence of the iodine atom coordinated to the aromatic ring where the oxygen atom is bonded. However, spectroscopic and magnetic anisotropy measurements that are out of the scope of this work would be needed to determine these parameters with accuracy and evaluate the effect of the donor atoms over the electronic and magnetic properties of these families. Calculated values together with the experimental data of the temperature-dependent magnetic susceptibility are plotted in Figure 3:

According to these calculations, the ground state function in the two-dysprosium derivatives is 84% of ±15/2 in **1-DMF(Dy)** and 96% of ±15/2 in **2-DMF(Dy)**. The first excited state is located at about 148 cm^{-1} in **1-DMF(Dy)**, whereas it appears closer in energy in **2-DMF(Dy)** (84 cm^{-1}). This evidences that the ground Kramer's doublet has a large contribution of the maximum M_J values and it is well isolated from excited states, allowing the observed slow relaxation of the magnetization in both cases. This description also provides an explanation compatible with the observed SIM behavior in the terbium complexes, which show a ground doublet with a tunneling splitting of 0.4 and 1.9 cm^{-1} in **1-DMF(Tb)** and **2-DMF(Tb)** respectively. In both cases, the ground doublet exhibits important contributions (> 40%) of +6 and -6 and a magnetic field is needed in order to split the +6 and -6 contributions. Further details about crystal-field parameters, energy levels and wave functions are available as supporting information. For the **1-DMF(Dy)** and **2-DMF(Dy)** compounds, the energy splitting between the basal state and the first exited state, is quite high compare to other systems, like the Dy(trensal) 50 cm^{-1} [31]. The closest system to compare with the systems here presented are the trinuclear dysprosium quinolinato reported by Chilton et al., with energies splitting of 106.1, 114.9 and 96.4 cm^{-1} for the Dy1, Dy2 and Dy3 centers, respectively[14].

Table S6. Ground multiplet energy level scheme (cm^{-1}) and main |M$_J$> contributions (more than 10%) to the wave function calculated for **1-DMF(Dy)**.

E(cm^{-1})	main |M$_J$> contributions
0	84% |±15/2>
148	88% |±13/2>
322	61% |±11/2>
376	23% |±9/2> + 10% |±7/2> + 32% |±1/2>
439	27% |±9/2> + 17% |±3/2> + 10% |±1/2>
618	10% |±9/2> + 18% |±7/2> + 23% |±5/2> + 11% |±3/2>
835	19% |±5/2> + 22% |±3/2> + 12% |∓1/2> + 10% |∓3/2>
911	16% |±9/2> + 26% |±7/2> + 14% |±5/2> + 13% |±3/2> + 17% |±1/2>

Table S7. Ground multiplet energy level scheme (cm^{-1}) and main |M$_J$> contributions (more than 10%) to the wave function calculated for **1-DMF(Tb)**.

E(cm^{-1})	main |M$_J$> contributions
0	40% |-6> + 40% |+6>
0.4	40% |-6> + 40% |+6>
201	36% |-5> + 36% |+5>
205	37% |-5> + 37% |+5>
294	39% |-4> + 39% |+4>
324	39% |-4> + 39% |+4>
413	35% |-3> + 35% |+3>
461	40% |-3> + 40% |+3>
524	43% |-2> + 43% |+2>
723	40% |-2> + 40% |+2>
769	38% |-1> + 38% |+1>
793	35% |-1> + 35% |+1>
820	75% |0>

Table S8. Ground multiplet energy level scheme (cm^{-1}) and main |M$_J$> contributions (more than 10%) to the wave function calculated for **1-DMF(Er)**.

1-DMF(Er)	
E(cm^{-1})	main |M$_J$> contributions
0	58% |±13/2> + 10% |±1/2> + 10% |∓11/2>
109	43% |±11/2> + 20% |∓13/2>
175	18% |±9/2> + 32% |±3/2> + 11% |±7/2>
233	27% |±5/2> + 17% |∓1/2> + 15% |±7/2> + 10% |∓7/2>
384	29% |±15/2> + 17% |±9/2> + 10% |±11/2> + 10% |±1/2>
471	27% |±15/2> + 19% |±1/2> + 12% |±13/2> + 10% |∓11/2>
617	26% |±15/2> + 22% |±9/2> + 14% |±3/2>
773	27% |±5/2> + 23% |±7/2> + 10% |±3/2> + 10% |∓7/2>

Table S9. Ground multiplet energy level scheme (cm^{-1}) and main |M$_J$> contributions (more than 10%) to the wave function calculated for **1-DMF(Ho)**.

E(cm^{-1})	main |M$_J$> contributions
0	33% |-8> + 33% |+8> + 15% |-5> + 15% |+5>
6	34% |-8> + 34% |+8> + 14% |-5> + 14% |+5>
136	25% |-4> + 25% |+4> + 12% |-7> + 12% |+7>
149	25% |-4> + 25% |+4> + 12% |-7> + 12% |+7>
253	24% |-3> + 24% |+3>
288	18% |-2> + 18% |+2> + 15% |-3> + 15% |+3> + 10% |0>
325	18% |-2> + 18% |+2> + 12% |-6> + 12% |+6>
376	17% |-6> + 17% |-1> + 17% |+1> + 17% |+6>
513	19% |+0> + 13% |-6> + 13% |+6> + 12% |-2> + 12% |+2>
524	17% |-6> + 17% |+6> + 12% |-7> + 12% |+7>
552	11% |-5> + 11% |+5> + 10% |-6> + 10% |+6>
577	11% |-7> + 11% |+7> + 10% |-1> + 10% |+1>
602	19% |-5> + 19% |+5>
640	16% |-5> + 16% |+5> + 14% |-2> + 14% |+2>
714	17% |-1> + 17% |+1> + 14% |-4> + 14% |+4> + 12% |-7> + 12% |+7>
738	21% |-1> + 21% |+1> + 11% |-3> + 11% |+3>
758	37%	0> + 12% |-4> + 12% |+4>

Table S10. Ground multiplet energy level scheme (cm^{-1}) and main |M$_J$> contributions (more than 10%) to the wave function calculated for **1-DMF(Dy)**.

E(cm^{-1})	main |M$_J$> contributions
0	96% |±15/2>
84	19% |±3/2> + 20% |±1/2> + 26% |∓1/2> + 11% |∓3/2>
435	81% |±13/2>
539	16% |±13/2> + 23% |±5/2> + 21% |∓3/2>
682	22% |±11/2> + 13% |±9/2> + 17% |±1/2> + 17% |∓7/2>
714	65% |±11/2> + 12% |∓7/2>
784	59% |±9/2> + 20% |∓7/2>
932	12% |±9/2> + 17% |±5/2> + 12% |±1/2> + 15% |∓3/2> + 14% |∓7/2>

Table S11. Ground multiplet energy level scheme (cm^{-1}) and main |M$_J$> contributions (more than 10%) to the wave function calculated for **1-DMF(Tb)**.

E(cm^{-1})	main |M$_J$> contributions
0	47% |-6> + 47% |+6>
2	48% |-6> + 48% |+6>
64	40% |-1> + 40% |+1>
69	49% |0> + 21% |-2> + 21% |+2>
405	34% |-5> + 34% |+5>
418	45% |-5> + 45% |+5>
459	24% |-3> + 24% |+3>
468	23% |-2> + 23% |+2> + 12% |-4> + 12% |+4> + 10% |-5> + 10% |+5>
589	39% |-4> + 39% |+4>
665	20% |-4> + 20% |+4> + 14% |-2> + 14% |+2> + 11% |-3> + 11% |+3>
702	28% |-3> + 28% |+3> + 14% |-4> + 14% |+4>
878	37% |0> + 26% |-2> + 26% |+2>
888	31% |+1> + 31% |-1> + 15% |+3> + 15% |-3>

Table S12. Ground multiplet energy level scheme (cm^{-1}) and main |M$_J$> contributions (more than 10%) to the wave function calculated for **2-DMF(Er)**. For the ground state, |M$_J$> contributions larger than 5% have been included.

E(cm^{-1})	main |M$_J$> contributions
0	76% |±13/2> + 9% |±7/2> + 5% |∓1/2>
42	12% |±15/2> + 41% |±11/2> + 10% |±3/2>
104	15% |±9/2> + 26% |±1/2>
159	20% |±15/2> + 12% |±5/2> + 20% |∓3/2>
244	42% |±15/2> + 20% |±11/2>
380	12% |±15/2> + 35% |±9/2> + 10% |±7/2> + 18% |∓7/2>
505	14% |±9/2> + 17% |±7/2> + 12% |±3/2> + 13% |∓5/2>
595	14% |±7/2> + 16% |±5/2> + 14% |±3/2> + 11% |±1/2> + 12% |∓1/2> + 11% |∓3/2> + 12% |∓5/2>

Table S13. Ground multiplet energy level scheme (cm^{-1}) and main |M$_J$> contributions (more than 10%) to the wave function calculated for **2-DMF(Ho)**.

E(cm^{-1})	main |M$_J$> contributions
0	47% |-8> + 47% |+8>
2	48% |-8> + 48% |+8>
109	24% |-1> + 24% |+1> + 20% |0>
111	27% |0> + 17% |-1> + 17% |+1> + 13% |-2> + 13% |+2>
220	22% |-3> + 22% |+3>
226	20% |-2> + 20% |+2> + 13% |-4> + 13% |+4>
310	16% |-7> + 16% |+7> + 12% |-3> + 12% |+3> + 10% |-1> + 10% |+1>
374	16% |-4> + 16% |+4> + 10% |-7> + 10% |+7>
422	23% |-7> + 23% |+7> + 10% |-4> + 10% |+4>
453	28% |-7> + 28% |+7> + 12% |-1> + 12% |+1>
468	20% |-4> + 20% |+4> + 10% |-2> + 10% |+2>
500	17% |-5> + 17% |+5> + 12% |-3> + 12% |+3>
539	22% |-6> + 22% |+6> + 18% |-5> + 18% |+5>
567	21% |0> + 16% |-6> + 16% |+6>
576	18% |-6> + 18% |+6> + 15% |-1> + 15% |+1> + 13% |-5> + 13% |+5>
605	17% |-5> + 17% |+5> + 16% |-3> + 16% |+3>
615	17% |-4> + 17% |+4> + 12% |-6> + 12% |+6> + 12% |-2> + 12% |+2>

S.4.3. Dynamic magnetic measurements (ac) for Na[Ln(5,7-Br$_2$q)$_4$]·DMF.

For the recrystallized dysprosium complex, **1-DMF(Dy)**, in the absence of an external dc field dynamic magnetic measurements (ac) have an out-of-phase signal, χ", which is frequency-dependent, although no maxima are observed at low frequencies, but increasing the applied frequencies maxima tend to appear but they are not completely defined. This could be due to the existence of fast relaxation of the magnetization through a quantum tunneling mechanism in the compound and/or to existence of intermolecular interactions between the Dy complexes. This phenomena can be avoid by the application of an external dc field that drives the magnetic levels away from the hyperfine avoided crossing region[32–35]. Then for **1-DMF(Dy)**, ac measurements performed under a smalls external dc fields of 100 G, 300 G, 500 G and 700 G, in which both χ' and χ" show a slower relaxation, and maxima are observed under all frequencies (Figures S16 – S19).

Analysis of the frequency dependence of the χ" peaks, for **1-DMF(Dy)** at 500 G, was performed assuming that Raman and Orbach relaxation processes exist (equations S1 and S2), but analyzing the two relaxation mechanism independently. A linear relation in all temperature range was achieved considering Raman relaxation mechanism, with a Raman constant, $B_{Raman} = 5.1 \times 10^{-10}$ Hz/K^9. A linear Arrhenius law for **1-DMF(Dy)** between the temperature ranges of 14.7 to 22.2 K was fitted, reflecting that Orbach relaxation mechanism is also present. In these temperature range and with a 500 G dc field, the fitting values for the energy barrier of the relaxation of the magnetization (U_{eff}) is 81 cm^{-1} and the pre-exponential factor is $\tau_0 = 4 \times 10^{-7}$ s. (see Figure S18).

Since for this compound it was not possible to obtain the B_{Raman} and U_{eff} at zero field, ac magnetic measurements at 100 G, 300 G and 700 G (Figures S16, S17, S19), were done in order to extrapolate the Raman constant and the energy barrier of the relaxation of the magnetization at zero dc field. The Raman constants obtained at the different dc fields are 4.4 x 10^{-10} Hz/K^9 (100 G); 4.7 x 10^{-10} Hz/K^9 (300 G); 5.1 x 10^{-10} Hz/K^9 (500 G) and 5.6 x 10^{-10} Hz/K^9 (700 G). A linear relation between the Raman constant and the dc field is obtained which allow extrapolating the B_{Raman} value at zero dc field 4.2 x 10^{-10} Hz/K^9. Considering only the high temperature data (above 12K), linear Arrhenius plots were obtained at the different fields, being the energy barriers (U_{eff}) 60 cm^{-1}, 68 cm^{-1} and 88 cm^{-1} at 100 G, 300 G and 700 G, respectively (Figures S16, S17 and S19). A linear relation was obtained between the energy barrier of the relaxation of the magnetization and the dc magnetic fields, which allows the extrapolation at zero dc field: $U_{eff} = 54$ cm^{-1} (Figure S20).

Equations for the ac magnetic properties analysis

Arrhenius equation:

$$\tau^{-1} = \tau_0^{-1} e^{\frac{-U_{eff}}{k_B T}}$$

Raman relaxation equation:

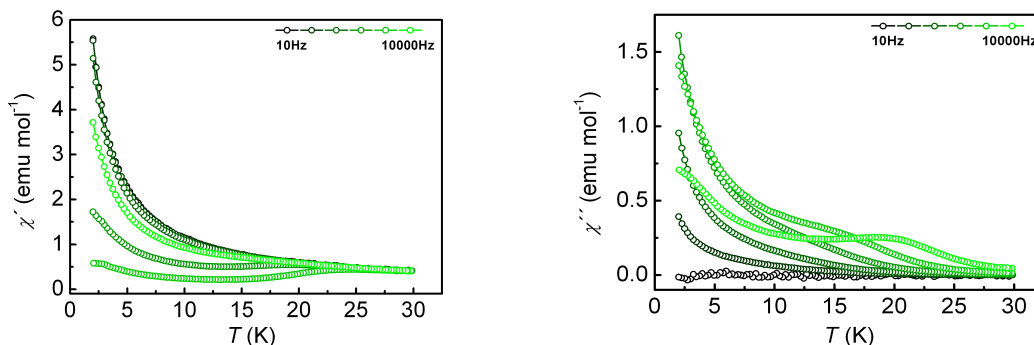$$\tau^{-1} = CT^n; where\ n = 9\ for\ a\ Kramers\ ion.$$

Figure S15. ac susceptibility measurements (in-phase and out-phase) obtained in the PPMS, at $H_{dc} = 0$ for the Na[Dy(5,7-Br$_2$q)$_4$]·DMF complex (**1-DMF(Dy)**).
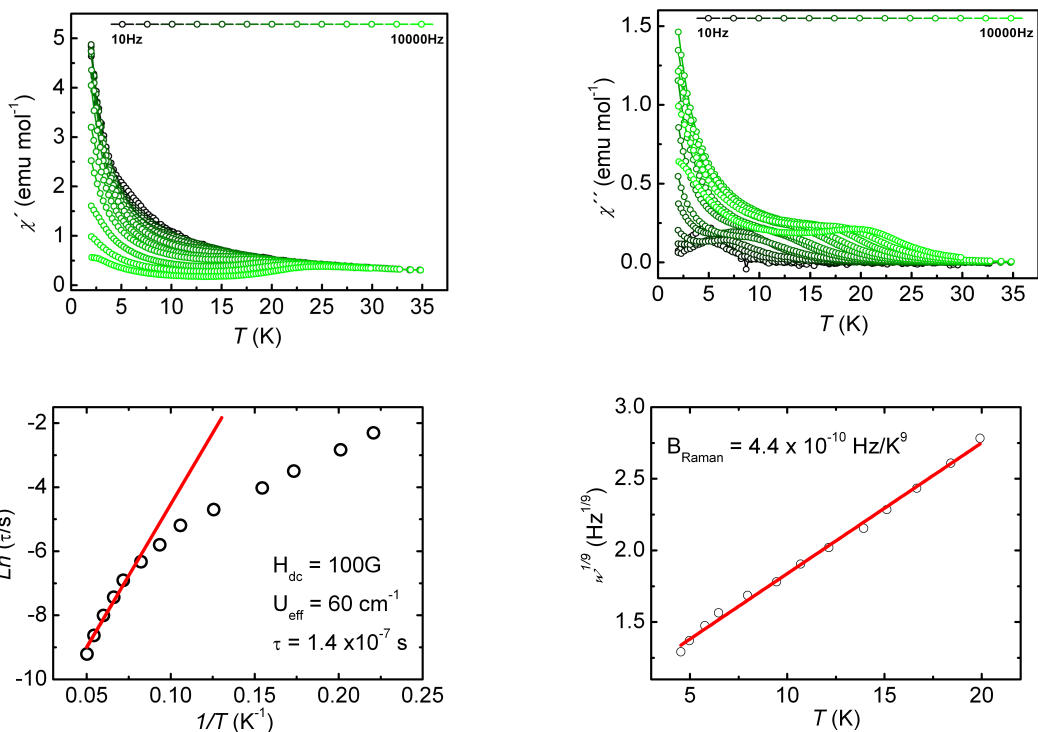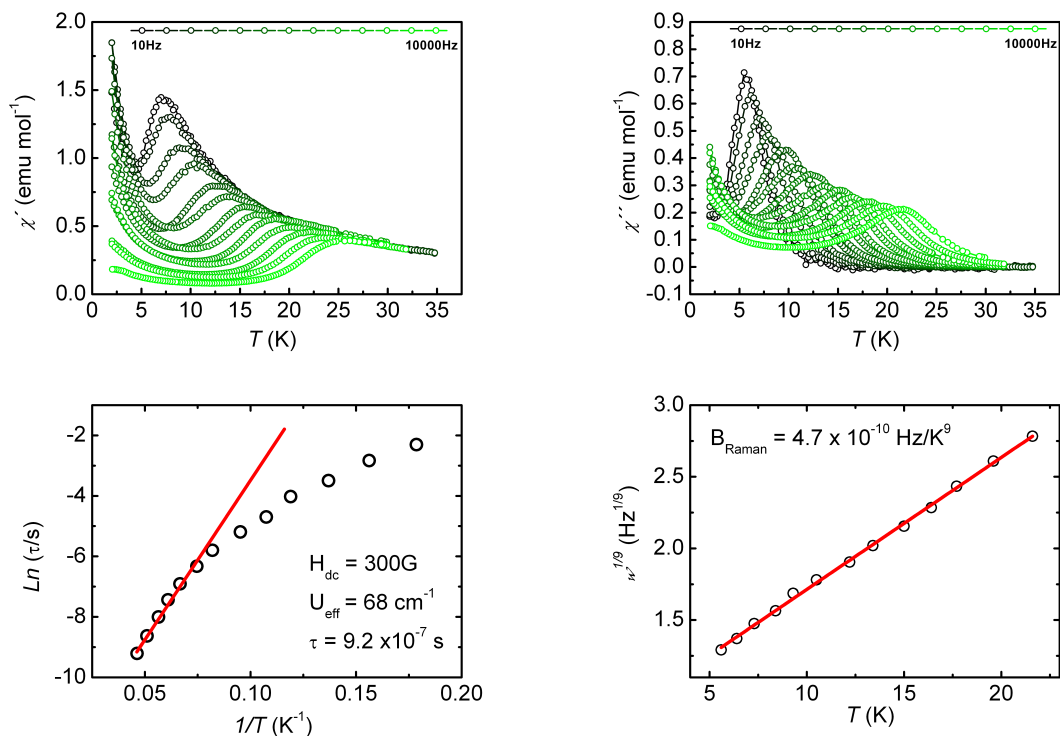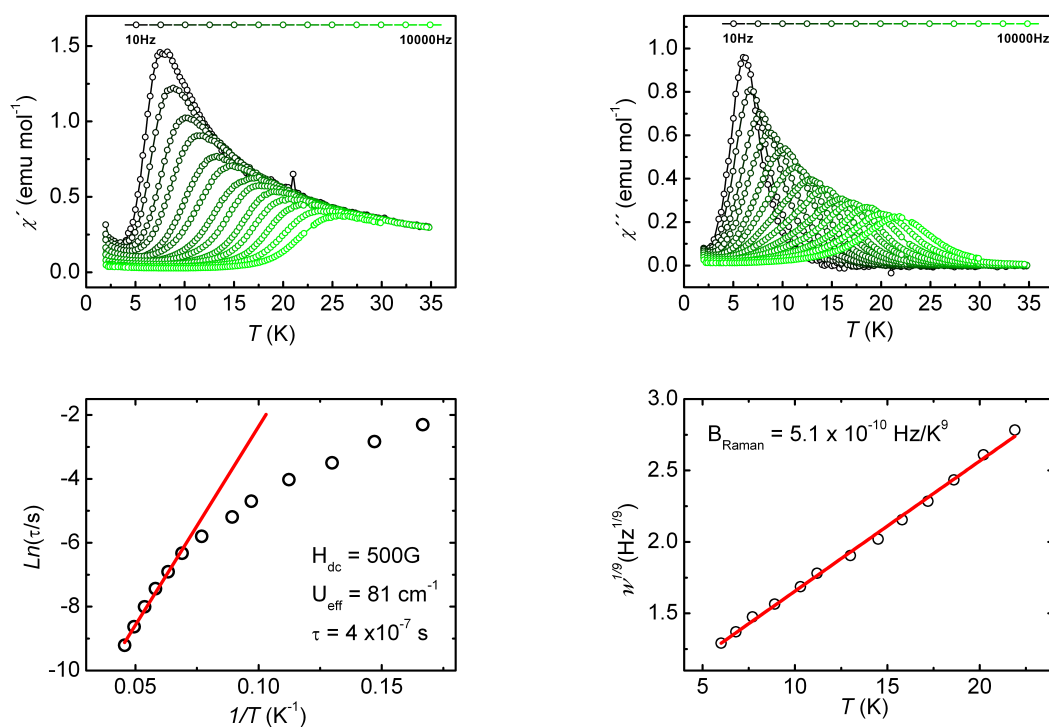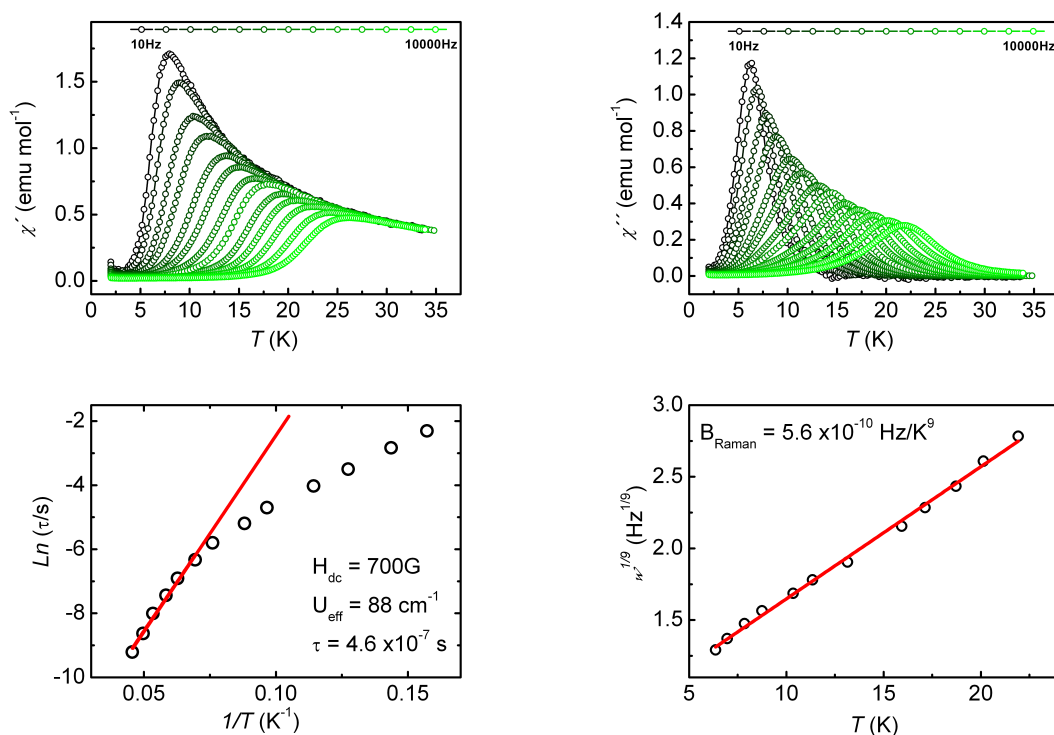
Figure S16. ac susceptibility measurements (in-phase and out-phase) obtained in the PPMS, at H_{dc} = 100G for the Na[Dy(5,7-Br$_2$q)$_4$]·DMF complex (**1-DMF(Dy)**). Orbach and Raman relaxation processes are also presented.

Figure S17. ac susceptibility measurements (in-phase and out-phase) obtained in the PPMS, at H_{dc} = 300G for the Na[Dy(5,7-Br$_2$q)$_4$]·DMF complex (**1-DMF(Dy)**). Orbach and Raman relaxation processes are also presented.

Figure S18. ac susceptibility measurements (in-phase and out-phase) obtained in the PPMS, at H_{dc} = 500G for the Na[Dy(5,7-Br$_2$q)$_4$]·DMF complex (**1-DMF(Dy)**). Orbach and Raman relaxation processes are also presented.

Figure S19. ac susceptibility measurements (in-phase and out-phase) obtained in the PPMS, at H_{dc} = 700G for the Na[Dy(5,7-Br$_2$q)$_4$]·DMF complex (**1-DMF(Dy)**). Orbach and Raman relaxation processes is also presented.
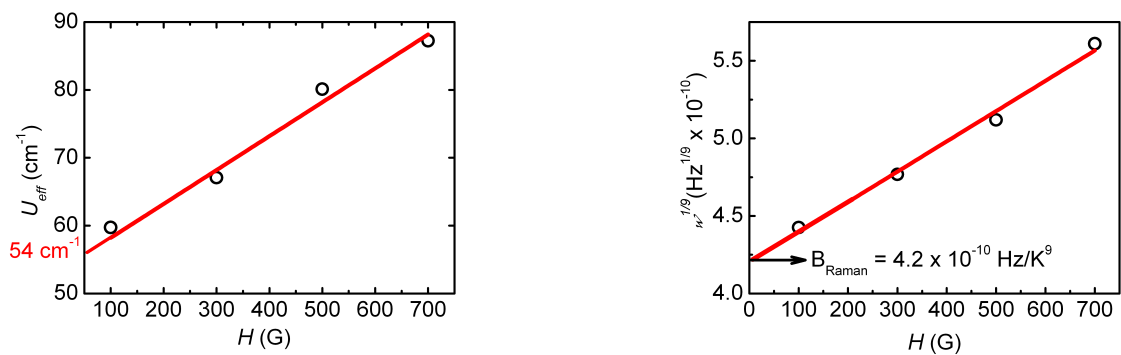
Figure S20. Extrapolation of the Raman constant (B_{Raman}) and energy barrier of the relaxation of the magnetization (U_{eff}) at zero dc field for **1-DMF(Dy)**.
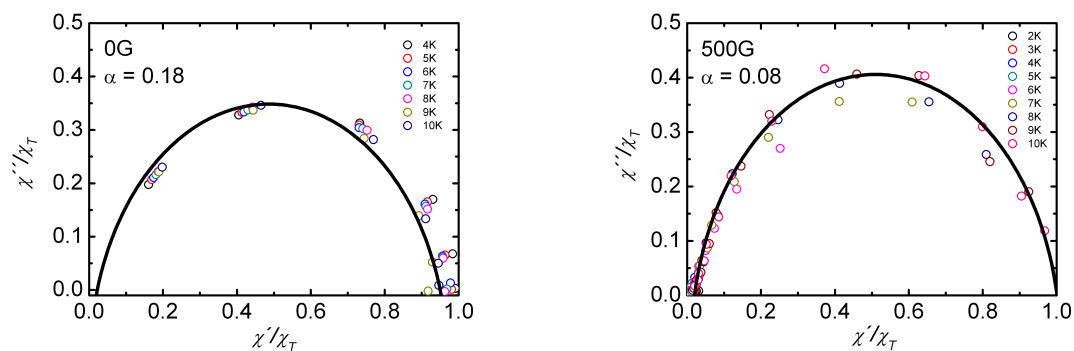
Figure S21. Argand plots at different temperatures (T = 2 – 10K) at dc fields of 0 and 500G for Na[Dy(5,7-Br$_2$q)$_4$]·DMF (**1-DMF(Dy)**).
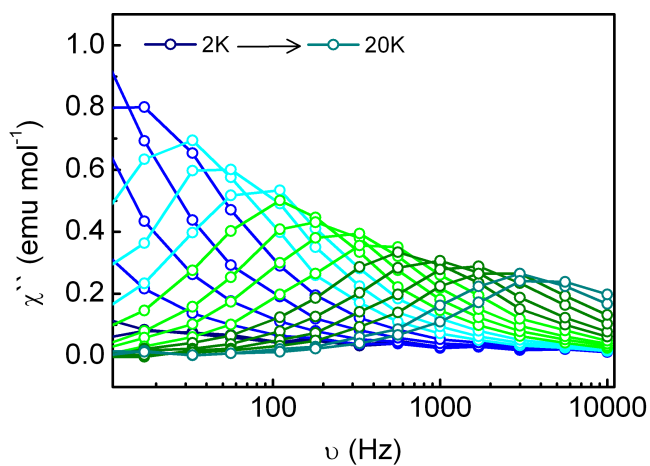
Figure S22. Frequency dependency of the ac susceptibility measurements (out-phase) obtained in the PPMS, at H_{dc} = 500G for the Na[Dy(5,7-Br$_2$q)$_4$]·DMF complex (**1-DMF(Dy)**).
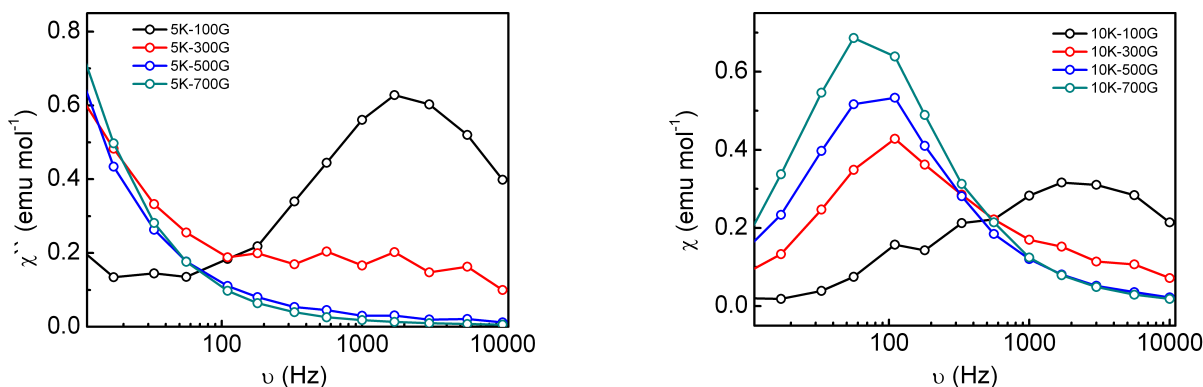
Figure S23. Frequencies dependencies of the ac susceptibility at different dc fields at two temperatures.

S.4.4. Dynamic magnetic measurements (ac) for Na[Ln(5,7-ClIq)$_4$]·DMF

For **2-DMF(Dy)**, in the absence of an external dc field dynamic magnetic measurements (ac) have an out-of-phase signal, χ'', which is frequency-dependent, although no maxima are observed at low frequencies. The absence of maxima at lower frequencies could be due to fast relaxation of the magnetization through a quantum tunneling mechanism. Increasing the applied frequencies, maxima start to appear for this compound (560 to 10000 Hz) allowing to fit independently the experimental data using Raman or Orbach relaxation mechanism[35–37] (Figure S24). Raman relaxation process have been neglected for some time, but recently some works have established the importance of considering the Raman relaxation in the dynamic magnetic properties[31,36,38]. We fitted independently the experimental data assuming Raman and Orbach relaxation mechanisms. Considering only Raman relaxation mechanism a linear fit is obtained with a B_{Raman} = 5.4 x 10^{-9} Hz/K^9. Also a lineal relation was obtained using an Arrhenius plot with an effective energy barrier amounts to 52 cm^{-1} and the pre-exponential factor is $\tau_0 = 1.0 \times 10^{-6}$ s (Figure S24). For **2-DMF(Dy)** under a dc field of 500 G, maxima appear at all frequencies. Considering a Raman type relaxation, as observed for the zero dc field measurement, a linear relation is obtained in all the temperature range with B_{Raman} = 6.9 x 10^{-9} Hz/K^9. Although, Orbach relaxation mechanism can be only fitted to an Arrhenius law in the high temperature range, as observed for **2-DMF(Dy)**. In these temperature range, the obtained U_{eff} values is 76 cm^{-1} and a pre-exponential factor, $\tau_0 = 1.2 \times 10^{-7}$ s. (Figure S25).

If the Raman and Orbach relaxations mechanism are compare, it is clear that the Raman is dominant over the Orbach since a better linear relation is obtained using Raman relaxation process. This can be understood since the energy barrier of **1-DMF(Dy)** (148 cm^{-1}) between the basal and first excited state which is much higher compare to the U_{eff} (54 cm^{-1}), which means the Orbach mechanism is mask by the Raman, implying that the relaxation take places via a two phonon through a virtual level. For **2-DMF(Dy)**, a similar behavior is observed, but the energy difference between the basal state and the first excited state is lower ($E_{15/2\rightarrow13/2}$ = 84 cm^{-1}) and with a U_{eff} = 52 cm^{-1}. The **2-DMF(Dy)** compound present SIM behavior at zero dc field and interestingly this is the system with the U_{eff} that it is closest to the energy difference between 15/2→13/2.

Nevertheless, as mention previously, the Orbach relaxation mechanism is mask by the Raman, but since a lineal relation is achieved at higher temperatures, Orbach relaxation processes cannot be discard. So considering Orbach relaxation mechanism an increase of the dc magnetic field leads to an increase of the U_{eff} value obtained by the Arrhenius fitting. The U_{eff} values obtained at zero dc field for the two dysprosium compounds are 54 cm^{-1} for **1-DMF(Dy)** (extrapolation) and 52 cm^{-1} for **2-DMF(Dy)** (Arrhenius fitting). These values are in the range of similar previously reported SIM magnets of dysprosium, like the trinuclear quinolinato dysprosium complex reported by Chilton el al., with a U_{eff} value of 61 cm^{-1} under the absence of dc field [14,16,39]. In addition, the fact that both systems have similar U_{eff} values at zero dc field indicates that the halogen substitution has a small effect on the energy barriers of the relaxation of the magnetization of these systems.

The ac behavior of these compounds with no observable maxima in the frequency dependent χ''(T) signal at zero field can be due to the highly distorted geometries of these complexes. These molecules are between three different geometries (square antiprism (sa), triangular dodecahedron (td) or bicapped trigonal prism (btp)) and as reported previously by Baldovi et al [40], the first and third type geometries are good candidates to obtained SIM behavior. This could explain the observed magnetic properties of the compounds since all the complexes are closest to the bicapped trigonal prism (according to the CShM´s values), which should present SIM behavior. If the CShM´s values of the dysprosium complexes (**1-DMF(Dy)** and **2-DMF(Dy)**) are compared together

complex **2-DMF(Dy)** has the CShM´s value closest to btp geometry, which is the compound that presents maxima at higher frequencies in the χ" (T) measurements under zero dc field.

Cole-Cole plots were used to extrapolate the alpha value (Figure S27). The distribution of the relaxation times can be studied by plotting χ" versus χ' in an Argand plot. The fit of the data to a general Debye model[41] results in almost ideal semicircles, in which a decrease of the α values is observed upon increasing the applied dc field. For **1-DMF(Dy)** at 0G and 500G, in temperature range 2 to 10 K, the α values are 0.18 and 0.04; for **2-DMF(Dy)** at 0G and 500G, in the same temperature range, the α values are 0.17 and 0.08. The low values of α suggest that a single Raman dominant relaxation mechanism exists for these complexes, since the Orbach mechanism is mask by the Raman for both compounds. It can be mentioned that at lower temperatures (2 – 4 K) some deviation exists in the Argand plots that can be attributed to the existence of quantum tunneling of magnetization (Figures S27).

Equations for the ac magnetic properties analysis

Arrhenius equation:

$$\tau^{-1} = \tau_0^{-1} e^{\frac{-U_{eff}}{k_B T}}$$

Raman relaxation equation:
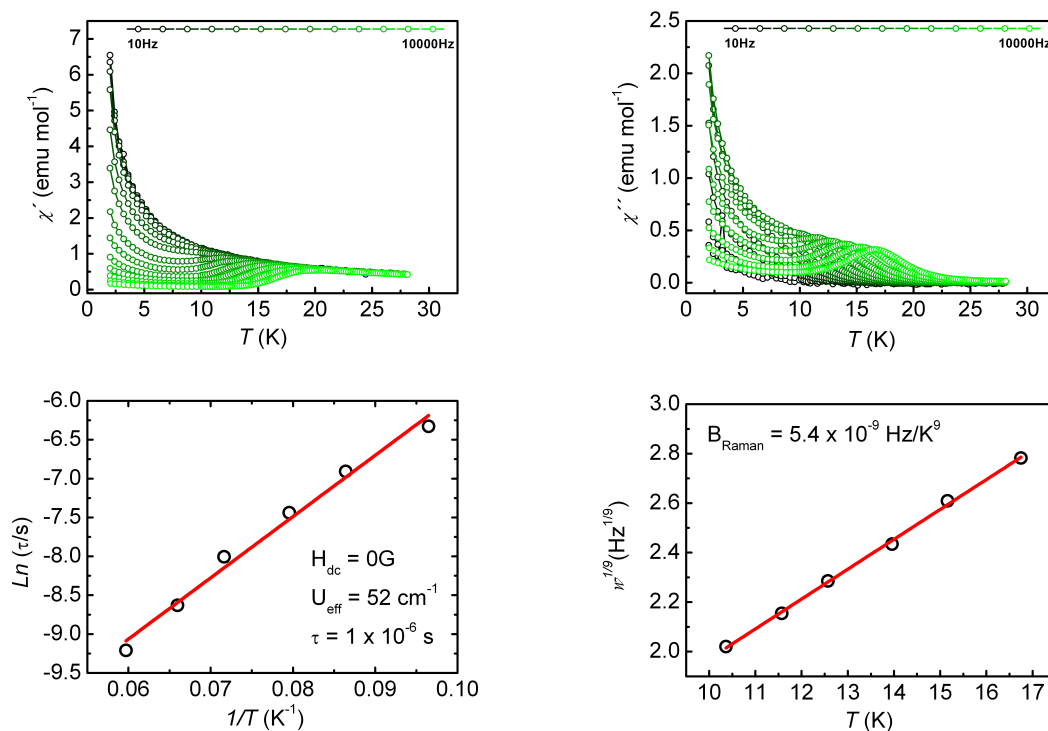
$$\tau^{-1} = CT^n; where\ n = 9\ for\ a\ Kramers\ ion.$$

Figure S24. ac susceptibility measurements (in-phase and out-phase) obtained in the PPMS, at H_{dc} = 0 G for the Na[Dy(5,7-ClIq)$_4$]·DMF complex (**2-DMF(Dy)**). Independently fitting of Raman and Orbach relaxation processes at H_{dc} = 0 G for Na[Dy(5,7-ClIq)$_4$]·DMF for frequencies above 560Hz.

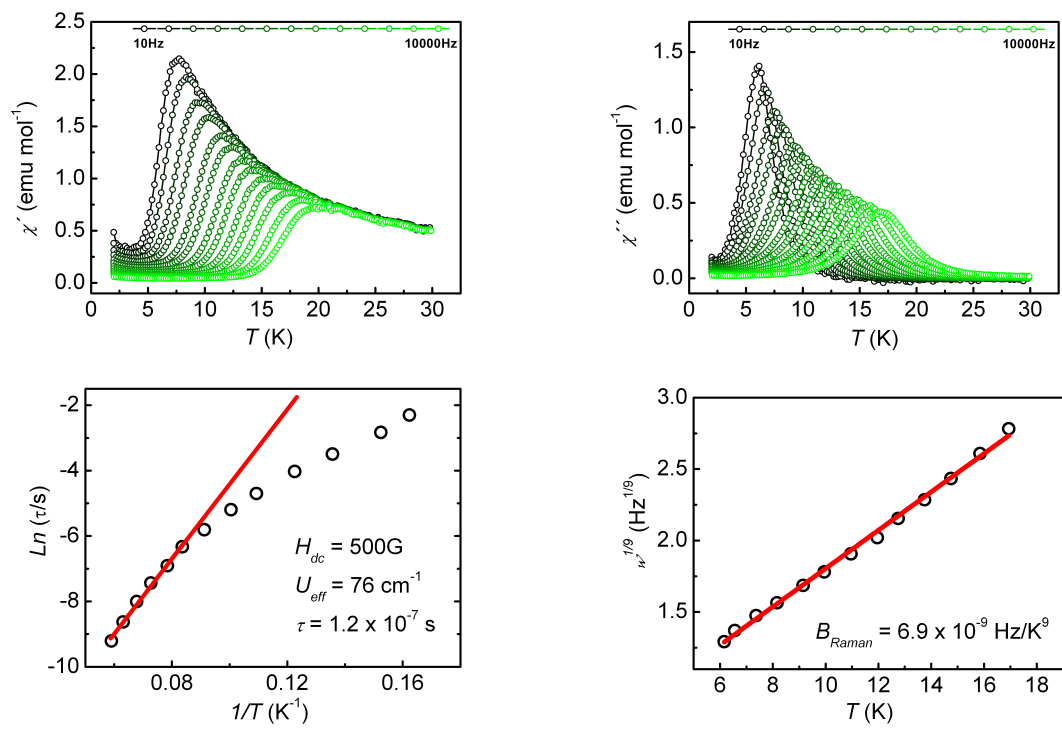**Figure S25.** ac susceptibility measurements (in-phase and out-phase) obtained in the PPMS, at H_{dc} = 500 G and H_{dc} = 500 G for the Na[Dy(5,7-ClIq)$_4$]·DMF complex (**2-DMF(Dy)**). Orbach and Raman relaxation processes are also presented.
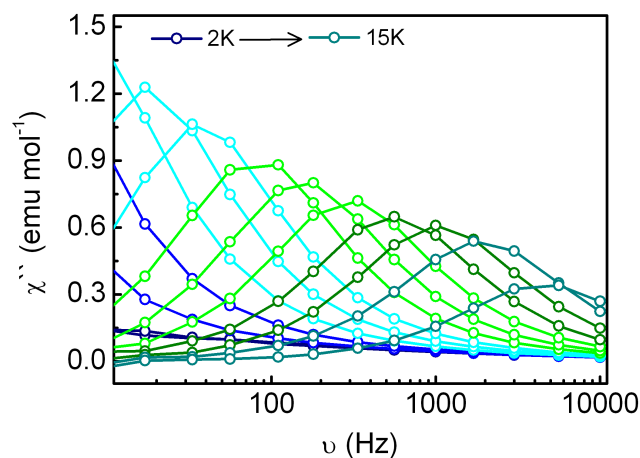

Figure S26. Frequency dependency of the ac susceptibility measurements (out-phase) obtained in the PPMS, at H_{dc} = 500G for the Na[Dy(5,7-ClIq)$_4$]·DMF complex (**2-DMF(Dy)**).
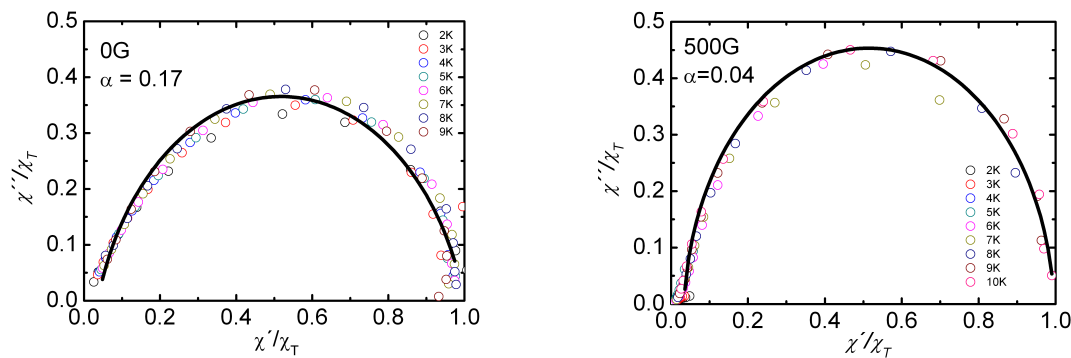
Figure S27. Argand plots at different temperatures (T = 2 – 10K) at dc fields of 0 and 500G for Na[Dy(5,7-ClIq)$_4$]·DMF (**2-DMF-(Dy)**).

S.4.5. Dynamic magnetic measurements (ac) for other lanthanoids

   The terbium complexes Na[Tb(5,7-X$_2$q)$_4$]·DMF, **1-DMF(Tb)** and **2-DMF(Tb)**, have no observable out-of-phase signal measuring at zero dc field, but measurements at 1500 G applied dc field revealed frequency-dependent signals in the plot of χ''(T) (no maxima), indicating a field-induced SIM behavior (Figure S28-S30). This is a commonly observed feature for Tb^{III} complexes because of the non-Kramer´s nature of the metal ion. Quantum tunneling of magnetization happens when states are brought into resonance and an extra-diagonal term create a quantum-tunneling gap. On the contrary, the Dy^{III} complexes, here presented, are Kramers ions where no tunneling gap is possible. Finally, it can be mentioned that the complexes of Er^{III} with both ligands, independently of the external dc field present no clear maxima are observed in out-of-phase signal, χ'' (Figure S29-31). The Ho complexes do not present out phase signal in ac magnetic measurements.
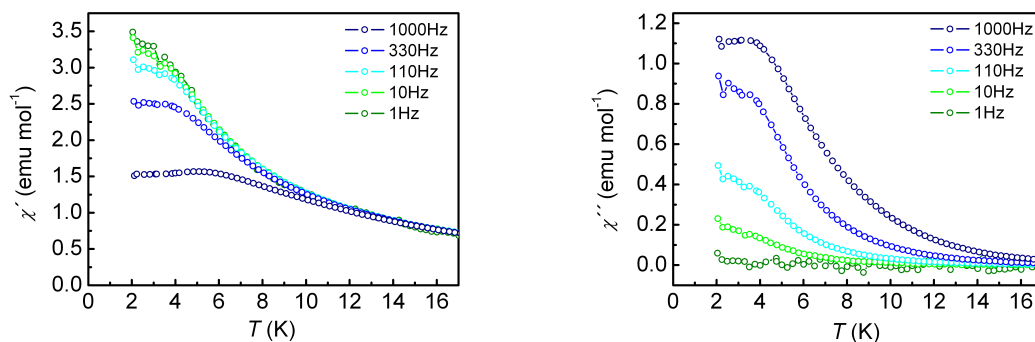

Figure S28. ac susceptibility measurements (in-phase and out-phase) obtained in the SQUID, at H$_{dc}$ = 1500 G for the Na[Tb(5,7-Br$_2$q)$_4$]·DMF (**1-DMF(Tb)**) complex.

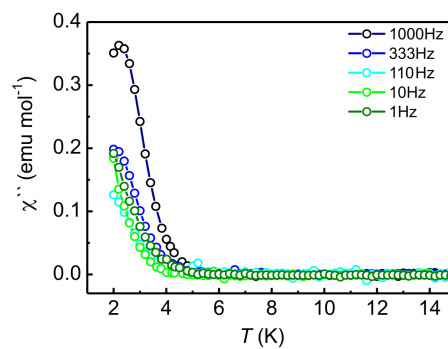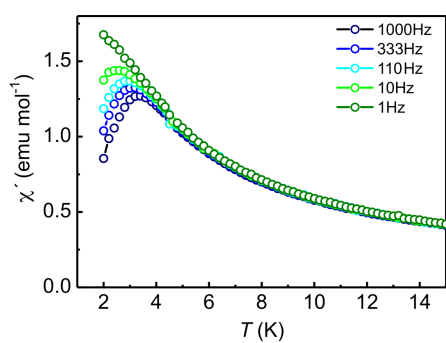**Figure S29**. ac susceptibility measurements (in-phase and out-phase) obtained in the SQUID, at H_{dc} = 2500 G for the Na[Er(5,7-Br$_2$q)$_4$]·DMF (**1-DMF(Er)**) complex.
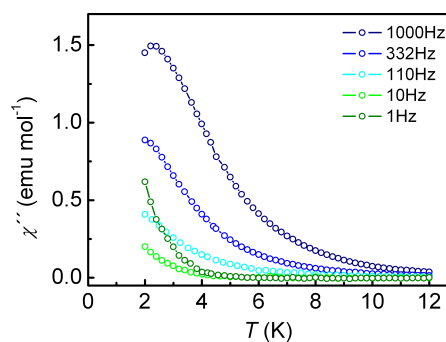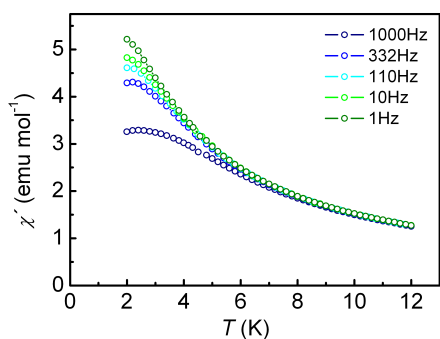

Figure S30. ac susceptibility measurements (in-phase and out-phase) obtained in the SQUID, at H_{dc} = 1500 G for the Na[Tb(5,7-ClIq)$_4$]·DMF (**2-DMF(Tb)**) complex.
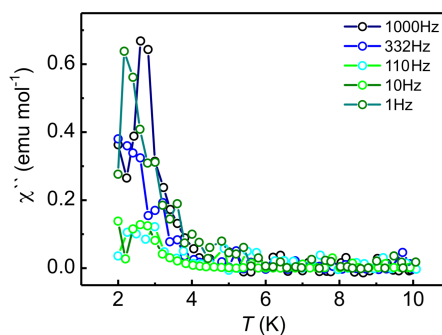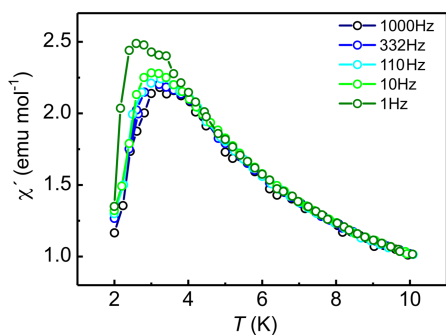

Figure S31. ac susceptibility measurements (in-phase and out-phase) obtained in the SQUID, at H_{dc} = 2500 G for the Na[Er(5,7-ClIq)$_4$]·DMF (**2-DMF(Er)**) complex.

S.5. FILM FABRICATION AND CHARACTERIZATION

S.5.1. Film fabrication

For the film fabrication, a glass substrates of 3 cm x 3 cm, were transferred to a vacuum chamber and evacuated. For each experiment, a ceramic crucible was filled with compounds **1(Dy)**, **2(Dy)**, **1-DMF(Dy)** and **2-DMF(Dy)**. We worked at a base pressure between 1 x 10^{-6} to 1 x 10^{-7} mbar, and in a temperature range between 180 and 200 °C for the 5,7-Br$_2$q compounds, and between 220 to 240 °C in the case of the 5,7-ClIq compounds. In the case of the compounds with 5,7-Br$_2$q ligands (**1(Dy)**; **1-DMF(Dy)**), neither the raw product nor the recrystallized, could be properly sublimated onto glass substrates. The film thickness was controlled by the rate of evaporation of 0.1 Å/s to a thickness of 20 nm, since a calibration was made using an Ambios Technology XP-1 perfilometer placed on a vibration isolation table.

Figure S32. Picture of the films of 20 nm obtained by sublimation onto glass substrates using the Na[Dy(5,7-ClIq)$_4$] (**2(Dy)**) complexes. Note that the substrate is placed on top of a paper towel after being deposited in the ultra-high vacuum system in the glovebox.

S.5.2. Film characterization

The deposited material was studied with different characterization techniques with the aim of determining if the chemical composition of the material is maintained upon sublimation (MALDI-TOF; FTIR; EDAX). Fourier transform infrared spectroscopy (FTIR) was done in a NICOLET 5700 in the range of 1600 – 650 cm^{-1} for the sublimated films. Matrix-Assisted Laser Desorption /Ionization Time of Flight Mass Spectrometry (MALDI-TOF) measurements on the deposited material were performed on a 5800 MALDI TOF (ABSciex) in negative (and positive) reflection mode (3000 shots at every position) in a mass range of 1000-3000 m/z. Isotopic distributed patterns were simulated using the mMass software (v. 5.5.0) and in all cases, well-resolved isotopic patterns consisting of mono-isotopic peaks separated by 1/z Da were obtained (no matrix was used). The Ln : X ratios (where X = Br, I, Cl) of the film samples were estimated by electron probe microanalysis (EPMA) performed with a Philips SEM XL30 equipped with an EDAX DX-4 microprobe. Surface diffraction to the sublimated films of the compounds at room temperature between 10° to 40° (2θ) were done. As for the AFM measurements, a Nanoscope Multimode (Veeco) atomic force microscope in tapping mode operation was used in the morphological study of the electrodeposited films. RMS roughness and average particle size were analyzed by using WSxM4 4.0 Develop 13.0 software, developed by Nanotec Electronics S.L. In a Quantum Design MPMS XL-5 SQUID magnetometer the dynamic magnetic properties of 0.9 mg of the deposited material of **2(Dy)** were measured in a temperature range of 2 – 30 K at different frequencies between 1 – 1000 Hz under a dc field of 500G.

MALDI-TOF experiments were done directly on the film deposited onto the substrate, both in the negative and positive modes, but no signal with the corresponding pattern and correct m/z was found for. Indeed, electron probe microanalysis of the deposited material ruled out the presence of the molecules since an incompatible Dy : Br ratio was found (theoretical, Dy : Br = 1 : 8 and experimental Dy : Br = 1 : 4).

In contrast, the compounds with the 5,7-ClIq ligands (**2(Dy)**; **2-DMF(Dy)**) were found to be suitable for sublimation under the same experimental conditions (P$_{base}$ = 1 x 10^{-6} mbar and T$_{sublimation}$ = 220 – 240 °C), obtaining yellow translucent films deposited on the glass substrates (Figure S32). MALDI-TOF in negative mode for the two compounds the experimental patterns matches with the theoretical predictions for the anionic part of the molecule, [Dy(5,7-ClIq)$_4$]$^-$ at m/z = 1380. In the positive mode a pattern corresponding to the Na$_2$[Dy(5,7-ClIq)$_4$]$^+$ fragment is observed at m/z = 1425. (Figure S33). Moreover, a correct atomic relation

between lanthanide (DyIII and ErIII), chlorine and iodine (Ln: Cl: I = 1: 4: 4) was found with electron probe microanalysis for the three complexes, 2-Dy, 4-Dy and 2-Er, deposited on the glass substrate, see Table S14.
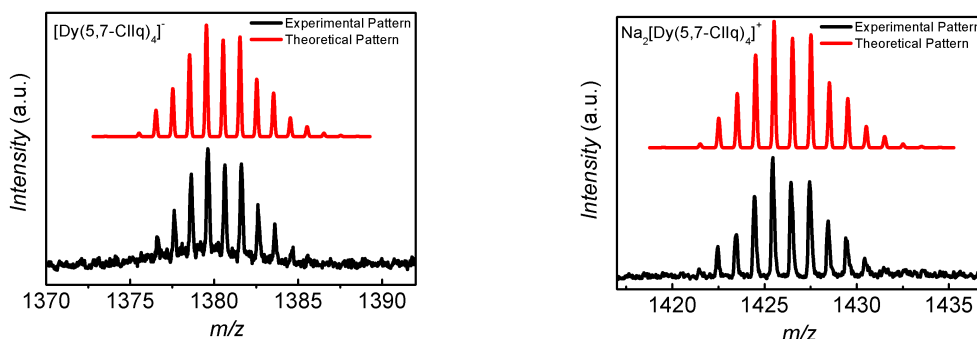

Figure S33. MALDI-TOF in negative and positive mode done to the deposited material of Na[Dy(5,7-ClIq)$_4$] (**2-DMF(Dy)**) compounds.

Surface Infrared spectra of the sublimated molecules were obtained in the range of 1600 to 650 cm^{-1} on the deposited material and were compared with the infrared spectra of the powder compounds in the same range. The same peaks of the IR spectra compound exist in the spectra of the deposited compounds. For example, at 954 cm^{-1} a clear asymmetric peak corresponding to the C-Cl vibrations appear as observed for IR spectra of the compound. The absence of the C-I peak at 926 cm^{-1} is also observed in the spectra of the compound, since its intensity is weak and causes the asymmetric shape of the Cl peak (Figure S34). Finally, the SXRD were done on the film and for the two complexes, no peaks are observed indicating that an amorphous material is deposited on the glass substrate under the sublimation conditions (Figure S35).
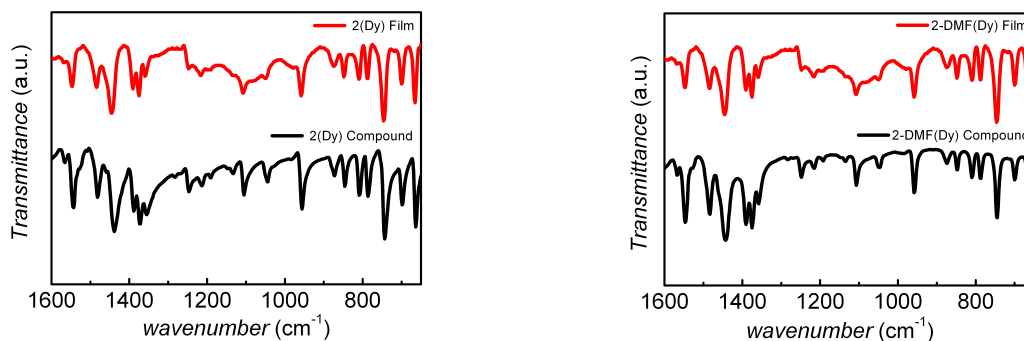

Figure S34. Surface infrared spectra of films of compounds **2(Dy)** and **2-DMF(Dy)** compared with the infrared spectra of the powder samples of the compounds.
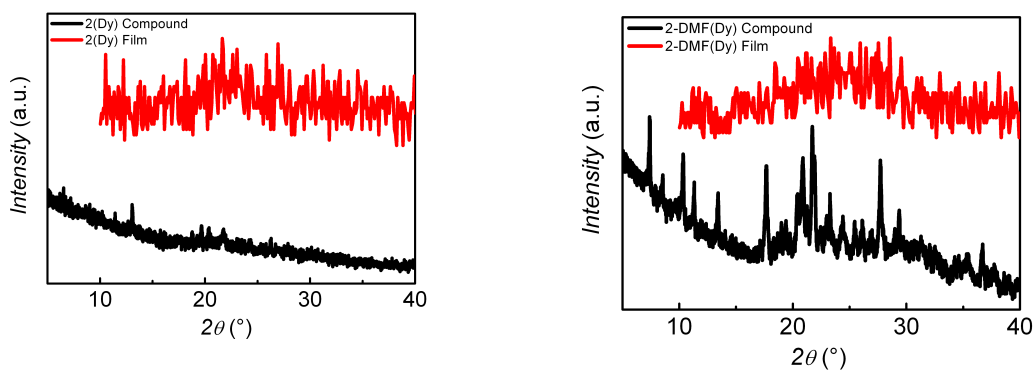
Figure S35. Comparison of the Surface X-Ray Difraction of films made with **2(Dy)** and **2-DMF(Dy)** compare with powder X-Ray Diffraction of the compounds **2(Dy)** (non-recrystallized material) and **2-DMF(Dy)** (recrystallized material).

Table S14. Atomic relation obtained of chlorine, iodine and dysprosium by electron probe microanalysis for the films using **2-Dy** and **2-DMF(Dy)** as starting materials.

	Cl-K	I-L	Dy-L
Na[Dy(5,7-ClIq)₄] **2(Dy)**	0.4710	0.4125	0.1175
Na[Dy(5,7-ClIq)₄]·DMF **2-DMF(Dy)**	0.4575	0.4175	0.1300

S.5.3. Magnetic properties of the dysprosium film

    The analysis of the dynamic magnetic of powdered compounds of **2-(Dy)** and **2-DMF(Dy)** at 500 G shows frequency dependent signals with differences in the maximum temperatures of 1.5 K moving to lower temperatures for the compounds without DMF. As observed in PPMS magnetic measurements of the $Na[Ln(5,7-X_2q)_4]\cdot DMF$ compounds Raman and Orbach relaxation mechanism exists. (Figures S36-S37).
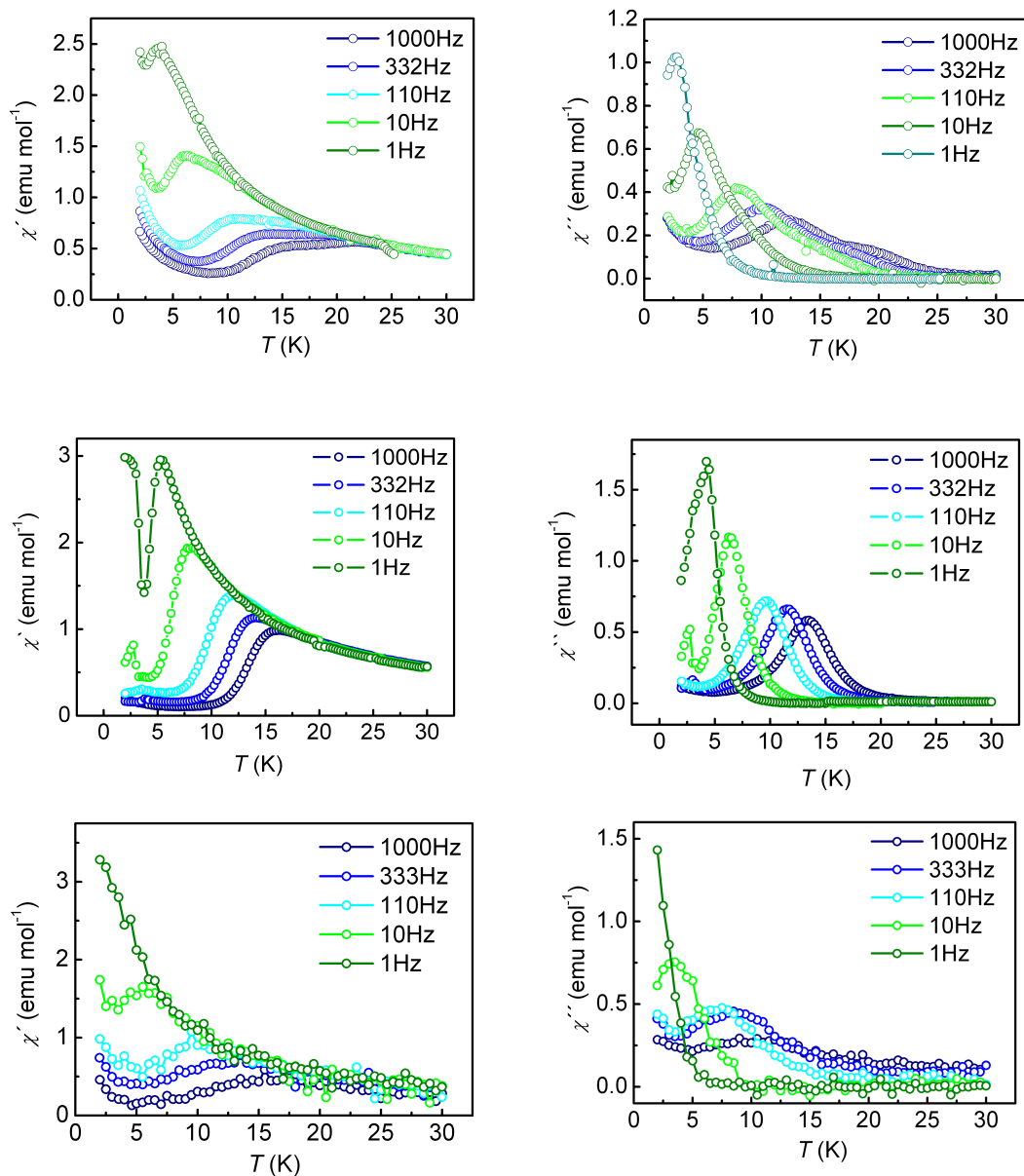

Figure S36. ac susceptibility measurements (in-phase and out-phase) obtained in the SQUID, at 500 G for the non-recrystallized $Na[Dy(5,7-ClIq)_4]$ (**2(Dy)**) complex (top), re-crystallized $Na[Dy(5,7-ClIq)_4]\cdot DMF$ (**2-DMF(Dy)**) complex (middle) and the sublimated $Na[Dy(5,7-ClIq)_4]$ (**2(Dy)**) film (bottom).
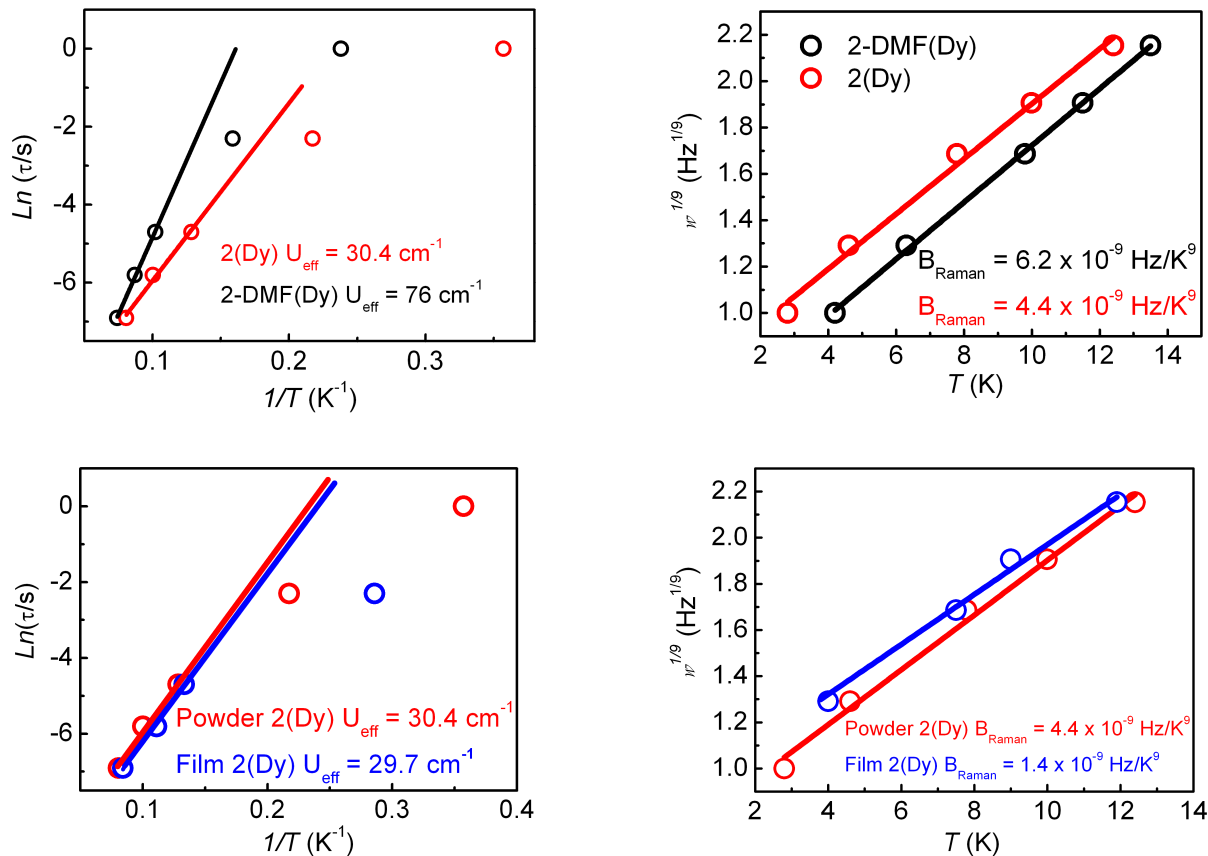
Figure S37. Orbach (Ln(τ) vs 1/T) and Raman ($w^{1/9}$ vs T) relaxation studies of Na[Dy(5,7-ClIq)$_4$]·DMF (**2-DMF(Dy)**, black) and Na[Dy(5,7-ClIq)$_4$] (**2(Dy)**, red) complexes compared with a film of **2(Dy)** (blue). The results show that both the powdered compound and the film have almost identically magnetic properties.

Figure S38. Argand plots at H_{dc} = 500 G for the Na[Dy(5,7-ClIq)$_4$]·DMF (left) and Na[Dy(5,7-ClIq)$_4$] (right) complexes before being sublimated.

S.6. REFERENCES

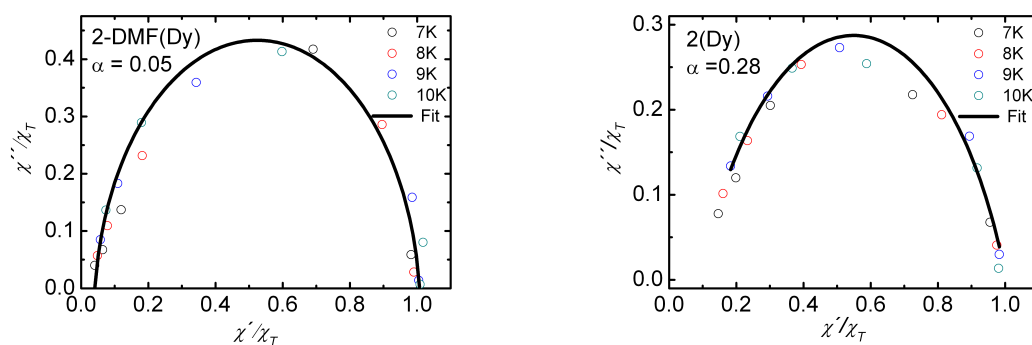(1) Van Deun, R.; Fias, P.; Nockemann, P.; Schepers, A.; Parac-Vogt, T. N.; Van Hecke, K.; Van Meervelt, L.; Binnemans, K. Rare-Earth Quinolinates: Infrared-Emitting Molecular Materials with a Rich Structural Chemistry. *Inorg. Chem.* **2004**, *43*, 8461–8469.

(2) Bisti, F.; Anemone, G.; Donarelli, M.; Penna, S.; Reale, A.; Ottaviano, L. Tetrakis Erbium Quinolinate Complexes , Electronic Structure Investigation. *Org. Electron.* **2014**, *15*, 1810–1814.

(3) Camargo, H.; Paolini, T. B.; Niyama, E.; Brito, H. F.; Cremona, M. New Rare-Earth Quinolinate Complexes for Organic Light-Emitting Devices. *Thin Solid Films* **2013**, *528*, 36–41.

(4) Sheldrick, G. M. The SHELX-97 Manual. *SHELXL-97, Program for Crystal Structure Refinement; University of Göttingen, Germany*. Program for Crystal Structure Refinement; University of Göttingen, Germany 1997.

(5) SHELXTL Version 5. *SHELXTL Version 5.1; Brucker AXS Madison, WI* **1998**.

(6) Wendlant, W. W. The Thermal Decomposition of the 5,7-Dihalo-8-Quinolinol Rare Earth Metal Chelates. *Anal. Chim. Acta* **1957**, *17*, 428–433.

(7) Casanova, D.; Cirera, J.; Llunell, M.; Alemany, P.; Avnir, D.; Alvarez, S. Minimal Distortion Pathways in Polyhedral Rearrangements. *J. Am. Chem. Soc.* **2004**, *126*, 1755–1763.

(8) Casanova, D.; Llunell, M.; Alemany, P.; Álvarez, S. The Rich Stereochemistry of Eight-Vertex Polyhedra: A Continuous Shape Measures Study. *Chem. - A Eur. J.* **2005**, *11*, 1479–1494.

(9) Kettles, F. J.; Milway, V. A.; Tuna, F.; Valiente, R.; Thomas, L. H.; Wernsdorfer, W.; Ochsenbein, S. T.; Murrie, M. Exchange Interactions at the Origin of Slow Relaxation of the Magnetization in {TbCu₃} and {DyCu₃} Single-Molecule Magnets. *Inorg. Chem.* **2014**, *53*, 8970–8978.

(10) Zhu, J.; Wang, C.; Luan, F.; Liu, T.; Yan, P.; Li, G. Local Coordination Geometry Perturbed β-Diketone Dysprosium Single-Ion Magnets. *Inorg. Chem.* **2014**, *53*, 8895–8901.

(11) Hänninen, M. M.; Mota, A. J.; Aravena, D.; Ruiz, E.; Sillanpää, R.; Camón, A.; Evangelisti, M.; Colacio, E. Two C3 -Symmetric Dy₃^{III} Complexes with Triple Di-μ-Methoxo-μ-Phenoxo Bridges, Magnetic Ground State, and Single-Molecule Magnetic Behavior. *Chem. - A Eur. J.* **2014**, *20*, 8410–8420.

(12) Li, X.; Wei, D. Y.; Huang, S. J.; Zheng, Y. Q. Syntheses and Characterization of Novel Lanthanide Adamantine-Dicarboxylate Coordination Complexes. *J. Solid State Chem.* **2009**, *182*, 95–101.

(13) Zhang, X. Q.; Lin, M. S.; Hu, B.; Chen, W. Q.; Zheng, L. N.; Wu, J.; Chen, Y. M.; Zhou, F. Y.; Li, Y. H.; Li, W. Anionic Lanthanide Complexes Supported by a Pyrrole-Based Tetradentate Schiff Base Ligand: Synthesis, Structures and Catalytic Activity toward the Polymerization of -Caprolactone. *Polyhedron* **2012**, *33*, 273–279.

(14) Chilton, N. F.; Deacon, G. B.; Gazukin, O.; Junk, P. C.; Kersting, B.; Langley, S. K.; Moubaraki, B.; Murray, K. S.; Schleife, F.; Shome, M.; Turner, D. R.; Walker, J. A. Structure, Magnetic Behavior, and Anisotropy of Homoleptic Trinuclear Lanthanoid 8-Quinolinolate Complexes. *Inorg. Chem.* **2014**, *53*, 2528–2534.

(15) Miralles, S. G.; Bedoya-pinto, A.; Baldoví, J. J.; Cañon-mancisidor, W.; Prado, Y.; Gaita-Ariño, A.; Mínguez Espallargas, G.; Hueso, L. E.; Coronado, E. Chloroquinolinate Lanthanoid Based Sublimable Single Ion Magnets: Deposition on Ferromagnetic Substrates. *Chem. Sci.* **2018**, *9*, 199–208.

(16) Woodruff, D. N.; Winpenny, R. E. P.; Layfield, R. A. Lanthanide Single-Molecule Magnets. *Chem. Rev.* **2013**, *113*, 5110–5148.

(17) Artizzu, F.; Bernot, K.; Caneschi, A.; Coronado, E.; Clemente-Juan, J. M.; Marchiò, L.; Mercuri, M. L.; Pilia, L.; Serpe, A.; Deplano, P. Synthesis, Structure, Spectroscopic Studies and Magnetic Properties of the Tetrakis(5,7-Dichloro-8-Quinolinolato)Gadolinium(III) Complex. *Eur. J. Inorg. Chem.* **2008**, 3820–3826

(18) Thielemann, D. T.; Wagner, A. T.; Lan, Y.; Anson, C. E.; Gamer, M. T.; Powell, A. K.; Roesky, P. W. Slow Magnetic Relaxation in Four Square-Based Pyramidal Dysprosium Hydroxo Clusters Ligated by Chiral Amino Acid Anions – a Comparative Study. *Dalt. Trans.* **2013**, *42*, 14794.

(19) Adhikary, A.; Sheikh, J. A.; Biswas, S.; Konar, S. Synthesis, Crystal Structure and Study of Magnetocaloric Effect and Single Molecular Magnetic Behaviour in Discrete Lanthanide Complexes. *Dalt. Trans.* **2014**, *43*, 9334–9343.

(20) Xue, S.; Chen, X.-H.; Zhao, L.; Guo, Y.-N.; Tang, J. Two Bulky-Decorated Triangular Dysprosium Aggregates Conserving Vortex-Spin Structure. *Inorg. Chem.* **2012**, *51*, 13264–13270.

(21) Chilton, N. F.; Langley, S. K.; Moubaraki, B.; Soncini, A.; Batten, S. R.; Murray, K. S. Single Molecule Magnetism in a Family of Mononuclear β-Diketonate Lanthanide(III) Complexes: Rationalization of Magnetic Anisotropy in Complexes of Low Symmetry. *Chem. Sci.* **2013**, *4*, 1719–1730.

(22) Yadav, M.; Mereacre, V.; Lebedkin, S.; Kappes, M. M.; Powell, A. K.; Roesky, P. W. Mononuclear and Tetranuclear Compounds of Yttrium and Dysprosium Ligated by a Salicylic Schiff-Base Derivative: Synthesis, Photoluminescence, and Magnetism. *Inorg. Chem.* **2015**, *54*, 773–781.

(23) Reddy, M. L. P.; Sivakumar, S. Lanthanide Benzoates: A Versatile Building Block for the Construction of Efficient Light Emitting Materials. *Dalton Trans.* **2013**, *42*, 2663–2678.

(24) Smart, P.; Mínguez-Espallargas, G.; Brammer, L. Competition between Coordination Network and Halogen Bond Network Formation: Towards Halogen-Bond Functionalised Network Materials Using Copper-Iodobenzoate Units. *CrystEngComm.* **2008**, *10*, 1335–1344.

(25) Metrangolo, P.; Neukirch, H.; Pilati, T.; Resnati, G. Halogen Bonding Based Recognition Processes: A World Parallel to Hydrogen Bonding. *Acc. Chem. Res.* **2005**, *38*, 386–395.

(26) Cardona-Serra, S.; Clemente-Juan, J. M.; Coronado, E.; Gaita-Ariño, A.; Camón, A.; Evangelisti, M.; Luis, F.; Martínez-Pérez, M. J.; Sesé, J. Lanthanoid Single-Ion Magnets Based on Polyoxometalates with a 5-Fold Symmetry: The Series $[LnP_5W_{30}O_{110}]^{12-}$ (Ln^{3+} = Tb, Dy, Ho, Er, Tm, and Yb). *J. Am. Chem. Soc.* **2012**, *134*, 14982–14990.

(27) Baldoví, J. J.; Borrás-Almenar, J. J.; Clemente-Juan, J. M.; Coronado, E.; Gaita-Ariño, A. Modeling the Properties of Lanthanoid Single-Ion Magnets Using an Effective Point-Charge Approach. *Dalton Trans.* **2012**, *41*, 13705.

(28) Baldoví, J. J.; Cardona-Serra, S.; Clemente-Juan, J. M.; Coronado, E.; Gaita-Ariño, A.; Palii, A. SIMPRE: A Software Package to Calculate Crystal Field Parameters, Energy Levels, and Magnetic Properties on Mononuclear Lanthanoid Complexes Based on Charge Distributions. *J. Comput. Chem.* **2013**, *34*, 1961–1967.

(29) Baldoví, J. J.; Gaita-Ariño, A.; Coronado, E. Modeling the Magnetic Properties of Lanthanide Complexes: Relationship of the REC Parameters with Pauling Electronegativity and Coordination Number. *Dalton Trans.* **2015**, *44*, 12535–12538.

(30) Baldoví, J. J.; Clemente-Juan, J. M.; Coronado, E.; Duan, Y.; Gaita-Ariño, A.; Giménez-Saiz, C. Construction of a General Library for the Rational Design of Nanomagnets and Spin Qubits Based on Mononuclear F-Block Complexes. The Polyoxometalate Case. *Inorg. Chem.* **2014**, *53*, 9976–9980.

(31) Lucaccini, E.; Sorace, L.; Perfetti, M.; Costes, J.-P.; Sessoli, R. Beyond the Anisotropy Barrier: Slow Relaxation of the Magnetization in Both Easy-Axis and Easy-Plane Ln(Trensal) Complexes. *Chem. Commun.* **2014**, *50*, 1648–1651.

(32) Baldoví, J. J.; Coronado, E.; Gaita-Ariño, A.; Gamer, C.; Giménez-Marqués, M.; Mínguez Espallargas, G. A SIM-MOF: Three-Dimensional Organisation of Single-Ion Magnets with Anion-Exchange Capabilities. *Chem. - A Eur. J.* **2014**, *20*, 10695–10702.

(33) Ishikawa, N.; Sugita, M.; Wernsdorfer, W. Nuclear Spin Driven Quantum Tunneling of Magnetization in a New Lanthanide Single-Molecule Magnet: Bis(Phthalocyaninato)Holmium Anion. *J. Am. Chem. Soc.* **2005**, *127*, 3650–3651.

(34) Ruiz, J.; Mota, A. J.; Rodríguez-Diéguez, A.; Titos, S.; Herrera, J. M.; Ruiz, E.; Cremades, E.; Costes, J. P.; Colacio, E. Field and Dilution Effects on the Slow Relaxation of a Luminescent DyO_9 Low-Symmetry Single-Ion Magnet. *Chem. Commun.* **2012**, *48*, 7916–7918.

(35) Campbell, V. E.; Guillot, R.; Riviere, E.; Brun, P.-T.; Wernsdorfer, W.; Mallah, T. Subcomponent Self-Assembly of Rare-Earth Single-Molecule Magnets. *Inorg. Chem.* **2013**, *52*, 5194–5200.

(36) Gómez-Coca, S.; Urtizberea, A.; Cremades, E.; Alonso, P. J.; Camón, A.; Ruiz, E.; Luis, F. Origin of Slow Magnetic Relaxation in Kramers Ions with Non-Uniaxial Anisotropy. *Nat. Commun.* **2014**, *5*, 4300.

(37) Dreiser, J. Molecular Lanthanide Single-Ion Magnets: From Bulk to Submonolayers. *J. Phys. Condens. Matter* **2015**, *27*, 183203.

(38) Pedersen, K. S.; Ungur, L.; Sigrist, M.; Sundt, A.; Schau-Magnussen, M.; Vieru, V.; Mutka, H.; Rols, S.; Weihe, H.; Waldmann, O.; Chibotaru, L. F.; Bendix, J.; Dreiser, J. Modifying the Properties of 4f Single-Ion Magnets by Peripheral Ligand Functionalisation. *Chem. Sci.* **2014**, *5*, 1650–1660.

(39) Aravena, D.; Ruiz, E. Shedding Light on the Single-Molecule Magnet Behavior of Mononuclear DyIII Complexes. *Inorg. Chem.* **2013**, *52*, 13770–13778.

(40)   Baldoví, J. J.; Cardona-Serra, S.; Clemente-Juan, J. M.; Coronado, E.; Gaita-Ariño, A.; Palii, A. Rational Design of Single-Ion Magnets and Spin Qubits Based on Mononuclear Lanthanoid Complexes. *Inorg. Chem.* **2012**, *51*, 12565–12574.

(41)   Dekker, C.; Arts, A.; de Wijn, H.; van Duyneveldt, A.; Mydosh, J. Activated Dynamics in the Two-Dimensional Ising Spin-Glass $Rb_2Cu_{1-x}Co_xF_4$. *Phys. Rev. Lett.* **1988**, *61*, 1780–1783.